Towards a monolithic process for open-access Fabry-Perot etalon cavities

by

James Maldaner

A thesis submitted in partial fulfillment of the requirements for the degree of

Master of Science
in
Microsystems and Nanodevices

Department of Electrical and Computer Engineering

University of Alberta

Abstract

This thesis describes the design, fabrication, morphological overview, optical characterization, and fluid infiltration of 'open-access', small mode-volume, and high quality-factor Fabry-Perot micro-cavities in the telecommunication range followed by the simulation of a-Si:H/SiO_2-based Bragg mirrors for sub-micron range devices.

First, we describe a monolithic approach to fabricating large-scale arrays of high-finesse and low-mode-volume Fabry-Perot microcavities with open access to the air-core. A stress-driven buckling self-assembly technique was used to form half-symmetric curved-mirror cavities, and a dry etching process was subsequently used to create micro-pores through the upper mirror. We show that the cavities retain excellent optical properties, with reflectance-limited finesse $\sim$2000 and highly predictable Laguerre-Gaussian modes. We furthermore demonstrate the ability to introduce liquids into the cavity region by micro-injection through the pores.

Secondly, we conducted a theoretical study on the potential use of amorphous hydrogenated silicon (a-Si:H) as the high-index material in quarter-wave-stack Bragg mirrors for cavity QED applications. Compared to conventionally employed Ta_2O_5, a-Si:H provides a much higher index contrast with SiO_2, thus promising significantly reduced layer-number requirements and a smaller mode volume. Silicon-based mirrors offer the additional advantage of providing a wide omnidirectional reflection band, which allows greater control of the background electromagnetic modes. From numerical studies at 850 nm,

we show that a-Si:H-based mirrors could enable significant improvements with respect to a Fabry-Perot cavity's maximum Purcell factor, cooperativity, and spontaneous emission coupling factor, and in addition, potentially reduced fabrication complexity. These advantages are anticipated to be even more compelling at longer wavelengths. Applications in sensing, optofluidics, and cavity quantum electrodynamics are envisioned.

...understand it as well as I may, my comprehension can only be an infinitesimal fraction of all I want to understand...

– Ada Lovelace [1]

Acknowledgements

First I would like to thank my supervisors, Dr. Ray DeCorby and Dr. Lindsay LeBlanc. Your acumen, expertise, and patience has been invaluable over the course of this work, and because of your guidance I've done more than I thought possible. To Dr. DeCorby, thank you for always pushing me toward a better and more precise understanding of optics and experimentation. Your help in guiding and editing this thesis was indispensable, the 'fits and starts' turned into a full story with your help. To Dr. LeBlanc, thank you supporting me through both my degrees and for encouraging me to become a better person and researcher. Thank you for sharing your experimental and theoretical knowledge and for your patience whenever I had a question, at the end of class or otherwise. Your uniquely kind leadership has always insured a welcome and safe environment for everyone, whether it be in the lab, classroom, office, or curling club.

To the past and present members of the Integrated Optics lab group, thank you all. Thank you to Sanaa al-Sumaidae for all your help on the fabrication and experimental portion, and for providing good conversation while we worked. Thank you to Tim Harrison and Graham Horning, for encouraging me to increase my presision in all realms of fabrication and for providing feedback when I was stuck on a problem. Thank you to Dr. Mohammadhossein Bitarafan for providing a welcoming environment to every new student and for providing a strong foundation upon which the experimental work in this thesis was built. Thank you to Clinton Potts, your thesis provided the theoretical

precursor for the cQED application of this work. Thank you to Dr. Seyed Azmayesh-Fard, Danny Pulikkaseril, Kyle Scheuer, and Lintong Bu for your patience as I "try to get the alignment just right" and for providing different perspectives on problems that arose.

To Dr. Gil Porat, thank you for your mentorship, both in career advice and with regards to professional skills. Thank you for the time, good humour, and the experience you shared. Thank you to all of the members of the LeBlanc Lab for making me feel welcome in the physics department and for sharing your incredible insight, knowledge, and curiosity with me. And thank you to all the nanoFAB staff for your expertise, these devices would not exist without your help. In particular, thank you to Scott Munro for your constant help with the Cobra system and to Stephanie Bozic for all the training and for the insight into the photo-lithography process.

Thank you to my family and friends for your constant encouragement and patience as I completed this. I'm a very different person now than when I started this degree, and I'm a better man because of all of you. To my partner, Marita Obst, who has listened to me intently during this whole project and is *the* very best editor I could have check my work: thank you so much for your love, intuition, and diligence. This thesis would not exist as it does without your help. To my Mom, Brenda Schulze, thank you for always believing in me, through all of my seasons. Thank you for always being interested in what I wanted to talk about at the kitchen island after school, this is in no small part because of you.

Thank you to the Quanta program for giving me the additional resources and opportunities to push myself, surrounded by incredible peers.

This research was funded by the Natural Sciences and Engineering Research Council, Alberta Innovates Technology Futures, Quanta Alberta, and the University of Alberta. Thank you for the opportunity to do this research.

Contents

1 Introduction **1**

1.1 Fabry-Perot micro-cavities 1

1.2 Contemporary Fabry-Perot cavities 4

1.3 Monolithic and open-access FPC fabrication 6

1.4 In this thesis 8

2 Optical cavity theoretical background **11**

2.1 Planar mirror Fabry-Perot cavities 11

2.2 Spherical mirror Fabry-Perot cavities 14

2.3 Distributed Bragg reflectors 18

2.4 Figures of merit for optical cavities 20

3 Fabrication of single-wafer open-access Fabry-Perot micro-cavities **24**

3.1 Design considerations and fabrication procedure 24

3.1.1 Device morphology 26

3.1.2 Mask Design 27

3.2 Fabrication details 28

3.3 Fabricated device morphology 32

4 Optical characterization of open-access Fabry-Perot micro-cavities **40**

4.1 Optical microscope experimental set-up 40

4.2 Cavity Device Characterization 41
4.3 Optical scans of fluid-filled devices 48

5 Theoretical study of silicon-based Bragg mirrors for sub-micron cQED applications 52

5.1 Introduction 53
5.2 Optical properties of optimized a-Si:H 54
5.3 Comparison of a-Si:H and Ta_2O_5-based QWS mirrors 57
5.4 Comparison of spontaneous emission in a-Si:H and Ta_2O_5-based microcavities 60
5.4.1 Numerical results for planar cavities 61
5.4.2 Numerical results for 3-dimensional cavities 62

6 Conclusion and Future Work 67

6.1 Summary 67
6.2 Future work 69

References 71

Appendix A Mask data 79

Appendix B Fabrication notes 81

Appendix C Yield 86

Appendix D Device configuration analysis 88

List of Tables

1.1 Historical cavity results with FOM for comparison. 7

3.1 RF magnetron sputtering parameters for a-Si and SiO_2 29

3.2 Sputtering parameters for the 'Teflon-like' low-adhesion layer (LAL) using Alcatel AMS110 31

3.3 Etching parameters for the Cobra Reactive Etch system 32

4.1 Extracted data from the spectral measurements for different hole configurations (N_h) on devices with D_d of 100 µm, D_p of 40 µm, and D_h of 4 µm. 44

4.2 Calculated data for different hole configurations (N_h) on devices with D_d of 100 µm, D_p of 40 µm, and D_h of 4 µm. 48

5.1 Predicted model cavity parameters for operation at 850 nm wavelength as detailed in the main text 60

A.1 Results subsection and corresponding cell from Table A.2. . . 79

A.2 Mask data 80

C.1 Yield and average height results 87

D.1 Measured data for different hole configurations (N_h) on devices with D_d of 100 µm, D_p of 40 µm, and D_h of 4 µm. 88

D.2 Measured data for different pattern diameters (D_p) on devices with D_d of 100 µm, D_h of 4 µm, and N_h of 6. 89

D.3 Calculated data for different pattern diameters (D_p) on devices with D_d of 100 µm, D_h of 4 µm, and N_h of 6. 89
D.4 Measured data for different hole sizes (D_h) on devices with D_d of 100 µm, D_p of 40 µm, and N_h of 6. 90
D.5 Calculated data for different hole sizes (D_h) on devices with D_d of 100 µm, D_p of 40 µm, and N_h of 6. 90

List of Figures

1.1 Schematic representation of a cQED system showing the atom-cavity coupling rate (g_0), the background emission (γ_{BG}), photon loss through scattering (κ_{L}), and photons extracted through the output mode (κ_0). Adapted from [5]. 2

1.2 Two examples of alternative cavities to FPCs. a)-b) are adapted from [11] and show a diamond nano-crystal coupled to a microdisk resonator. c) is adapted from [12] and shows a PC defect microcavity. The inset shows a simulated resonant mode in the PC cavity. 3

1.3 Examples of contemporary classical FPC fabrication techniques. a) Two wafers bonded with a spacer. Adapted from [21]. b) Fibre aligned with a flat DBR. Adapted from [26]. c) Two fibres, with curved mirrors formed on their end facets, aligned using piezoelectric actuators. Adapted from [32]. . . . 5

1.4 Illustration of (from left to right) the established FPC fabrication process: Deposition of bottom mirror, application and patterning of LAL, deposition of top mirror, and buckling of the top mirror. 6

1.5 a) Microscope image of a FPC and the connected wave guide (with computer model of the device inset). b) Transmission spectra of the device shown in a). c) SEM image of a dome with a hole etched using FIB milling. d) Transmission spectra of the device shown in c). e) Fundamental mode of the device shown in c). Adapted from [40]. 8

2.1 Basic FPC geometry, showing the progress of a single beam reflecting inside the cavity. The incident beam i is assumed to be of unity amplitude and also to be linearly polarized in either the parallel or perpendicular direction relative to the plane of incidence. The reflected beams are denoted with a, b, c, d and the transmitted beams are denoted with α, β, γ. The positive superscripts indicate the incident beam was travelling left to right, the negative superscript indicates that the beam was travelling right to left, with the subscripts indicating at which mirror the interaction occurred. Adapted from [44]. 12

2.2 Example transmitted irradiance of a FPC *vs*. incident light frequency. Labelled are the free-spectral-range (ν_{f}), longitudinal mode spacing ($\Delta\nu_{\mathrm{q}}$), the full-width half-max linewidth ($\Delta\nu_{1/2}$), and the higher-order mode spacing ($\Delta\nu_{\mathrm{q,l,m}}$). 13

2.3 a) Various defects possible in FPCs. b) The effect of non-parallelism on a cavity. Adapted from [47]. 14

2.4 Basic spherical FPC geometry. a) shows a perspective of 3D spherical mirrors with a bounded ray retracing itself. Adapted from [53]. b) Gaussian beam parameters with an exaggerated beam showing the minimum beam waist, beam waist, Rayleigh range, and radius of curvature along the optical axis. Adapted from [54]. 15

2.5 The top row shows the theoretical Laguerre-Gaussian (left panel) and Hermite-Gaussian resonant modes (right panel). The bottom panel shows the connection between IG, HG and LG modes. Adapted from [56–58]. 17

2.6 Bragg reflector mechanics, showing a 3.5 layer Bragg mirror. Adapted from [61]. 19

3.1 New fabrication process, in which access holes are etched into pre-buckled domes. The dimensions are not to scale and the process is depicted from top left to bottom right. The top row is a copy of Figure 1.4 which depicts the existing process. Subsequently, the PR is spun-cast and patterned, the top mirror is etched using RIE, and finally the PR is removed using an acetone bath. 26

3.2 Mask pattern of a 3-hole buckled device. Red signifies the LAL and green or blue indicate the etch pattern. Three device configuration parameters are indicated on the far left device: D_{p}, D_{h}, and D_{d}. The remaining three images show representative D_{p} configurations. 27

3.3 Left: Reflected irradiance of the bottom mirror measured using VASE and compared to the simulated reflectance from a 4-period a-Si/SiO_2 mirror with the properties discussed in the text. Right: A SEM image taken at an angle where the top mirror has been cleaved such that the 4 periods of a-Si and SiO_2 are visible. Where the top mirror adheres to the bottom mirror can be seen in the double-thick layer at the bottom. 30

3.4 Many buckled domes with etch holes. a) shows multiple adjacent domes successfully etched and buckled b) shows a dome with 4 etch holes, c) shows a dome with 12 etch holes. 33

3.5 Two representative devices showing the effect of the etched hole size on the buckled device morphology. a) is a buckled device with D_{d} of50 µm, D_{p} of 20 µm, D_{h} of 4 µm, and N_{h} of 3. b) is a buckled device with D_{d} of100 µm, D_{p} of 40 µm, D_{h} of 5 µm, and N_{h} of 6. Deviations from the predicted profile is shown in both devices. Each row contains the data for one device, where i) shows a surface plot with gradient shading of the ZYGO scan and contour maps, normalized to the device height, projected behind and below. ii) shows the same aggregated, overlaid data for all radial directions extracted from profilometer scan in blue, the predicted buckled profile in red, the predicted profile of spherical dome with the effective radius of curvature at the top of the buckle is shown in green, the black bars indicate where the etch holes are patterned in ideally aligned devices. 37

3.6 The same morphological visualizations as described in Figure 3.5 Two representative devices showing the effect of the pattern size on the buckled device morphology. a) is a buckled device with D_d of 100 µm, D_p of 20 µm, D_h of 4 µm, and N_h of 12. b) is a buckled device with D_d of 100 µm, D_p of 60 µm, D_h of 4 µm, and N_h of 12. Deviations from the predicted profile were observed in both devices. 38

3.7 The same morphological visualizations as described in Figure 3.5. Two representative devices showing the affect of the etch hole size on the buckled device morphology. a) is a buckled device with D_d of 100 µm and no etch holes used as a control. b) is a buckled device with D_d of 100 µm, D_p of 40 µm, D_h of 4 µm, and N_h of 12. Relatively small deviations from the predicted profile were observed in both devices. 39

4.1 Experimental spectral set-up. The insets show more detail of the junction points on the set-up with relevant labels. 42

4.2 The same morphological visualizations as described in Figure 3.5 except for ii) a removal of the circular fit plots and the addition of a CMOS camera image showing the device with the fundamental mode superimposed, showing the mode location in the dome relative to the etched holes. Three representative devices to illustrate the affect of the number of holes on the buckled device morphology. a) is a buckled device with D_{d} of 100 µm and no etch holes used as a control. b) is a buckled device with D_{d} of 100 µm, D_{p} of 40 µm, D_{h} of 4 µm, and N_{h} of 6. c) is a buckled device with D_{d} of 100 µm, D_{p} of 40 µm, D_{h} of 4 µm, and N_{h} of 8. Only slight deviations from the predicted profile were observed in any of these devices. 43

4.3 Spectral scans of devices with each row showing N_{h} of 0, 6 and 8 respectively. i) The $\mathrm{TEM}_{0,0}$ mode with the intensity profile and a Gaussian profile overlayed, ii) The fundamental mode from the high-resolution spectral scan with the Lorentzian profile overlayed, iii) The low-resolution spectral scan where the higher order TEM modes inset were taken with the CMOS camera and converted to a contour map normalized to the maximum irradiance up to the fifth order. 47

4.4 (a) Screen-shot image of a cavity just prior to infiltration by IPA. The laser frequency is fixed, and the cavity is resonating in a high-order transverse mode pattern. (b) Image captured after fluid infiltration, showing the cavity resonating in a fundamental mode. Sequential dispensing and evaporation of droplets caused repeatable transition between these two states. In both images, scattered light can be seen 'leaking' through many of the etch holes. Note that the laser is incident from beneath the sample, so that the images correspond to transmitted light collected by the camera. 49

4.5 a),b) Show optical scans of the dome filled with IPA. c),d) Microscope images showing the small device filled (d) and empty (c) 51

5.1 a) Refractive index and (b) extinction coefficient versus wavelength assumed for a-Si:H (blue solid curves) and Ta_2O_5 (red dashed curves) films in our modeling study. In part (b), experimental data points for a-Si:H are from the references indicated in the legend. Refs: A is [91], B is [95], C is [98] 55

5.2 Predicted reflectance (a) and potential transmittance (b) at 850 nm wavelength versus number of periods in a QWS mirror employing a-Si:H (blue circles) and Ta_2O_5 (red diamonds) as the high-index layers. 58

5.3 (a) Predicted normal-incidence reflectance for the 5-1/2-period a-Si:H-based (blue solid line) and 13-1/2-period Ta_2O_5-based QWS mirrors. (b) Reflectance for TM-polarized light versus incident angle at the design wavelength $\lambda_0 = 850$ nm, for the a-Si:H- (blue solid line) and Ta_2O_5-based (red dashed line) mirrors 59

5.4 (a) Schematic diagram of a half-symmetric 'buckled dome' microcavity in cross-section, with an embedded horizontally-oriented dipole emitter indicated by the black arrow. The lower (planar) and upper (curved, with effective radius of curvature R_{oc}) mirrors are assumed to be identical N_B-1/2-period QWS (b) Planar model for the dome microcavity. 60

5.5 Local density of modes (LDOM) density plots versus in-plane wave-vector component, for transverse electric (TE) (solid lines) and transverse magnetic (TM) (dashed lines) polarization. The simulations were performed at an off-resonant wavelength $\lambda_0 = 860\,\text{nm}$. (a) Results for the Ta_2O_5-based cavity, predicting significant radiation into both free-space propagating ($k_{\|}/k_0 < 1$) and QWS guided modes. (b) Results for the a-SI:H-based cavity, showing that radiation into free-space modes is negligible and radiation into guided modes is reduced. 63

5.6 (a) Mode field intensity for the fundamental mode of the Ta_2O_5-based cavity. (b) Relative dipole emission rate versus wavelength for the Ta_2O_5-based cavity. The inset is a zoomed-in portion of the plot, far removed from the resonance. (c), (d) Show analogous plots for the a-Si:H-based cavity. 65

B.1 Alignment marks used and an example of how it appears on a lithography alignment screen. 84

B.2 Attempted buckles where you can see raised areas around the etch holes. 84

B.3 Images related non ideal LAL layers. 84

B.4 Microscope images of domes during buckling and after they exploded off from being exposed to too much heat. 85

B.5 Buckled dome with etch holes, some of which do not fully penetrate the dome. 85

B.6 Open access was first confirmed using a SEM image. Here you can see a buckled dome that was broken with the electrons passing through the etched hole. 85

C.1 This shows how the height of the domes depends more on the location of the dome than on the dome configuration with the lighter color indicating taller devices. The image is rotated for formatting reason but the cells are as follows: Top right - 1, bottom right - 2, middle top - 3, middle bottom - 4, bottom left - 6 87

D.1 Images of the tightly patterned devices. a) SEM image of the etched holes for the tight pattern. The clear overlap in the etch profiles of adjacent holes indicates a significant amount of material is removed. b) High order mode for 8 hole configuration, here the holes interfering with the mode is clear. c) Microscope image showing the same device as b) under a microscope. . . 89

Symbols

A	Absorption.
A_{B}	Bragg absorption.
$\mathcal{A}(\phi)$	Airy shape function.
c	Speed of light in vacuum.
C	Cooperativity.
d	Film thickness.
d_{h}	High-index thickness.
d_{l}	Low-index thickness.
D_{d}	Dome diameter.
D_{h}	Hole diameter.
D_{min}	Minimum device diameter.
D_{p}	Pattern diameter.
E	Young's modulus.
E_0	Normalization factor for the electric field.
$\vec{E}$	Electric vector field.
F_{I}	Inhibition factor.
F_{p}	Purcell factor.
$\mathcal{F}$	Finesse.
$\mathcal{F}_{\mathrm{D}}$	Defect finesse.
$\mathcal{F}_{\mathrm{R}}$	Reflectance finesse.
g_0	Atom-cavity coupling rate.
H_x	Hermite polynomial of order x.
I	Irradiance.
I_{i}	Input irradiance.

I_{r}	Reflected irradiance.
I_{t}	Transmitted irradiance.
J_0	Bessel function of order zero and first kind.
k	Wave number.
K_{F}	Coefficient of finesse.
L	Effective cavity length.
L_x^y	Generalized Laguerre polynomial of order (x, y).
M_1	Mirror 1.
M_2	Mirror 2.
n	Index of refraction.
n_0	Input index.
n_{h}	High-index material index of refraction.
n_{l}	Low-index material index of refraction.
n_{s}	Substrate index.
N_{B}	Number of layers.
N_{h}	Number of holes.
q	Longitudinal mode number.
Q	Quality factor.
R	Reflectance.
R_{B}	Bragg reflectance.
R_{oc}	Radius of curvature.
$\mathrm{R}(z)$	Radius of curvature of the phase front of a Gaussian beam.
T	Transmission.
T_{P}	Potential transmittance.
v	Poisson's ratio.
V_{m}	Mode volume.
w_0	Minimum beam waist.
$w(z)$	Beam waist.
z	Axial position in the cylindrical coordinate system.
z_{R}	Rayleigh range.
β	Photon coupling efficiency.
γ_0	Free-space emission.

γ_{BG} Cavity background emission rate.

γ_{c} Cavity mode emission.

δ Maximum deflection of buckle.

δ_{p} Mirror penetration.

$\Delta(\rho)$ Vertical Deflection.

$\Delta\zeta$ On-axis longitudonal phase delay.

$\Delta\lambda_{\mathrm{B}}$ Stop band of Bragg mirror.

$\Delta\nu_{1/2}$ Full-width half-max of fundamental mode.

$\Delta\nu_{\mathrm{q}}$ Mode frequency spacing between longitudinal modes.

$\Delta\nu_{\mathrm{q,l,m}}$ Mode frequency spacing between higher order modes..

ϵ Ellipticity parameter.

ϵ_0 Permittivity of a vacuum ($\epsilon_0 \approx 8.845 \times 10^{-12}\,\mathrm{F/m}$).

$\zeta(z)$ Gouy phase.

θ_{i} Input angle.

ϑ Angular position in the cylindrical coordinate system.

κ Photon decay rate of the cavity (Chapter 1).

κ Extinction coefficient.

κ_{L} photon decay-rate of the cavity lost.

κ_0 photon decay-rate of the cavity into the output mode.

κ_{l} Low-index material extinction coefficient.

κ_{h} High-index material extinction coefficient.

λ Wavelength.

λ_{B} Bragg wavelength.

μ First Zero of Bessel function of order zero and first kind.

ν Frequency.

ν_{f} Free-spectral-range.

ν_{q} Longitudinal resonant frequency of mode q.

$\nu_{\mathrm{q,l,m}}$ Higher order resonant frequency of mode q, l, m.

ρ Radial position in the cylindrical coordinate system.

σ Film Stress.

σ_{c} Critical film stress.

ϕ Phase shift.

Abbreviations

AZ P4620	MicroChemical's AZ P4620 Resist.
cQED	cavity quantum electrodynamics.
DBR	distributed Bragg reflector.
FIB	focused ion beam.
FOM	figure of merit.
FPC	Fabry-Perot cavity.
FWHM	full-width at half-maximum.
HG	Hermite-Gaussian.
ICPRIE	inductively coupled plasma reactive ion-etching.
IG	Ince-Gaussian.
IPA	isopropal alcohol.
LAL	low-adhesion layer.
LDOM	local density of modes.
LG	Laguerre-Gaussian.
NIR	near infrared.
PC	photonic crystal.
PR	photo resist.
QWS	quarter-wave stack.
RIE	reactive-ion etching.
RTA	rapid thermal annealing.
SEM	scanning electron microscope.
TEM	transverse electromagnetic mode.
VASE	variable-angle spectroscopic ellipsometer.
ZYGO	ZYGO NewView 5000 optical profilometer.

Chapter 1

Introduction

1.1 Fabry-Perot micro-cavities

The Fabry-Perot cavity (FPC) is a remarkably simple, flexible, and powerful optical component that has been pivotal in many scientific and technological fields. These cavities are the archetypal optical cavity resonator, first described and analysed at the end of the nineteenth century by two graduate students: Charles Fabry and Alfred Perot [2–4]. Classic FPCs are entirely described using the reflectance and separation between their inward facing mirrors, and the cavity mode energy stored as a standing-wave electric field between mirrored walls. The FPC can contain the field both temporally through interference inside the cavity, and spatially through the cavity geometry and mirror properties, quantified respectively by the quality-factor (Q) and the mode-volume (V_{m}).

An interesting use of these Fabry-Perot cavities is for cavity quantum electrodynamics (cQED): the study of confined light interacting with a quantum-emitter (or rather light-emitter or simply emitter). To illustrate the most basic configuration (as outlined in several places [6, 7]), consider a single two-level atomic emitter inside a FPC with a high quality-factor and a small mode-volume such as the one shown in Figure 1.1. Three rate parameters dictate the cavity-atom interactions: the atom-cavity coupling rate (g_0), background emis-

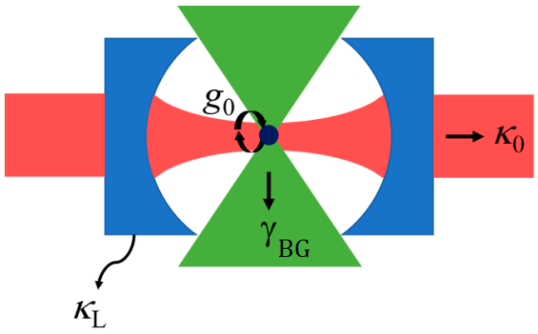

Figure 1.1: Schematic representation of a cQED system showing the atom-cavity coupling rate (g_0), the background emission (γ_{BG}), photon loss through scattering (κ_{L}), and photons extracted through the output mode (κ_0). Adapted from [5].

sion (γ_{BG}), and photon loss ($\kappa = \kappa_{\mathrm{L}} + \kappa_0$) through scattering and absorption losses (κ_{L}) and photons extracted through the output mode (κ_{L}). The most interesting physics is held in the strong-coupling regime, where $g_0 > (\kappa, \gamma_{\mathrm{BG}})$, but due to practical limitations, fabricating cavities in this regime is a significant challenge [6]. However, cavities within the Purcell regime with $\kappa \gg g_0 \gg \gamma_{\mathrm{BG}}$ can be fabricated and can significantly modify the emission of an atom within a cavity. This is quantified with a dimensionless factor of single-atom cooperativity $C = g_0^2/(\kappa\gamma_{\mathrm{BG}}) = \gamma_{\mathrm{c}}/(2\gamma_{\mathrm{BG}})$; here, $2\gamma_{\mathrm{c}}$ is the cavity mode emission rate. This leads to the critical atom number $N_0 = 1/C$ which is the number of atoms required to significantly modify the cavity field. For cavities within the Purcell regime, $C \gg 1$ is possible and has been shown in a variety of devices [6], allowing for significant modification of the local density of modes of a emitter inside the cavity.

The enhancement of the emission rate into the cavity mode over that into free space (γ_0) is called the Purcell effect, which is usually expressed through the idealized Purcell factor. This enhancement for a emitter which is perfectly aligned spatially, spectrally, and in terms of polarization with the cavity mode is given by $F_{\mathrm{p}} \equiv \gamma_{\mathrm{c}}/\gamma_0 = (3/4\pi^2)Q_{\mathrm{eff}}/(V_{\mathrm{m}}/\lambda^3)$. There is also the possibility for

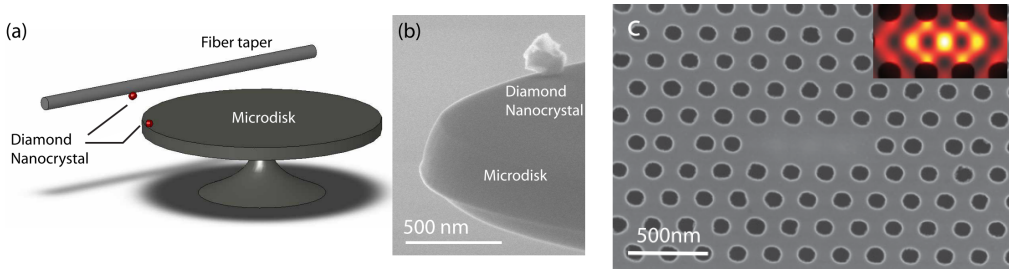

Figure 1.2: Two examples of alternative cavities to FPCs. a)-b) are adapted from [11] and show a diamond nano-crystal coupled to a micro-disk resonator. c) is adapted from [12] and shows a PC defect microcavity. The inset shows a simulated resonant mode in the PC cavity.

an inhibition of the background emission, which is significant in particular for sealed microcavities [8], however it is heavily dependent on the cavity geometry and therefore has no analytic form. If the inhibition of background modes is not significant (*i.e.* $\gamma_0 \sim \gamma_{\mathrm{BG}}$) then the cooperativity can be approximated from $C \sim F_{\mathrm{p}}/2$.

Optical cavities coupled with emitters have become a valuable tool with which to study and harness the interaction of atoms and light [6, 7]. Applications of these emitter-cavity systems include single-photon sources [9] and Λ-style quantum memory [10]. A common aim of most micro-cavity work is to maximize the single-atom cooperativity [6]. This emerging application simultaneously requires high quality-factor (Q) and low mode-volume (V_{m}). It follows then that it is essential to cQED applications that the emitter is at the peak field location, and therefore access to the cavity mode is essential for most applications of cQED.

Truly open-access, high quality-factor, and low mode-volume cavities remain challenging to fabricate [6]; however, significant effort in the past several decades has been given to optimising these cavities.

1.2 Contemporary Fabry-Perot cavities

Several micro-cavity designs have been developed using either periodic dielectric structures or by coupling to surface modes guided by total internal reflection.

Whispering gallery mode cavities (devices that use the surface modes of micro-devices as cavity modes [11, 13]) have been fabricated in spheres, disks, cylindrical resonators, and toroids [14]. These devices use total internal reflection (TIR), and therefore can achieve extremely high Q but generally at the cost of a large mode-volume. In addition, due to TIR, the devices must be solid state, and therefore post-fabrication tuning is generally difficult. Also due to their solid state nature, emitters can only interact with the evanescent wave from the modes, shown for example, in Figure 1.2 a).

There are two types of contemporary cavities formed with periodic media: solid state dielectric structures or 'air-core' cavities with distributed Bragg reflectors as mirrors (classical FPC). Several solid state periodic structures have been demonstrated including micro-pillars [15], micro-ring resonators which use circular wave-guides as cavities [16], and photonic crystals (PCs), such as those that embed a defect or other emitter in a two dimensional dielectric structure [12, 17] for example the one shown in Figure 1.2 c). However, these cavities have a similar issue to those described above as they cannot be easily tuned nor can media or analytes be added to the high-mode-field region of the cavity.

The primary issues with the alternative cavity configurations, such as those shown in Figure 1.2, is their solid-state nature. While these alternative cavity configurations display many analogous phenomena, it is challenging to tune the cavity after it is fabricated, and only evanescent waves are accessible to emitters. The 'air-gap' of classic FPCs allows for applications involving the bi-

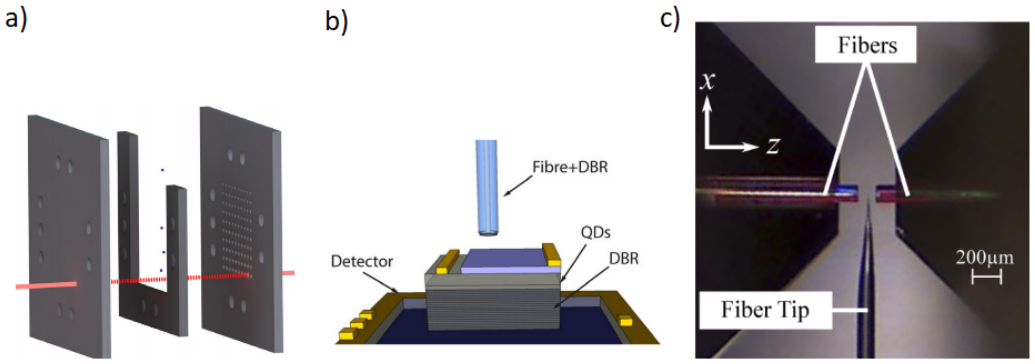

Figure 1.3: Examples of contemporary classical FPC fabrication techniques. a) Two wafers bonded with a spacer. Adapted from [21]. b) Fibre aligned with a flat DBR. Adapted from [26]. c) Two fibres, with curved mirrors formed on their end facets, aligned using piezoelectric actuators. Adapted from [32].

stability of the cavities [18] or post-fabrication tuning of the cavity length [19].

Contemporary classical FPCs are often fabricated by bonding two mirror-coated chips [20–22] or manually aligning fibre end-facet mirrors, such as those in Figure 1.3. The fibre-based cavities are aligned through translation stages or through v-grooves manipulated using shear piezoelectric actuators [23–31]. Examples of devices fabricated with these methods are shown in Figure 1.3.

Both methods deposit two separate mirrors which require individual alignment, significantly increasing the complexity and expense of fabrication. For example, fibre end-facet cavities fabricated with manual assembly impose a minimum distance between the mirrors, thereby limiting cavity characteristics such as cavity length and mode volume. Conversely, these methods produce open-access cavities which allow emitters or fluids to interact with the cavity mode.

Further theoretical studies into FPCs is ongoing, with several studies outlining techniques to further improve the coupling in a cavity and emitter system. Experimental studies report overlapping standing-waves in doubly resonant cavities being used to further enhance atom-cavity coupling [32]. Promising theoretical models exploit the birefringent nature of the micron-

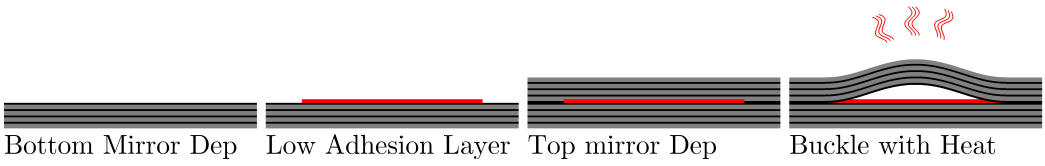

Figure 1.4: Illustration of (from left to right) the established FPC fabrication process: Deposition of bottom mirror, application and patterning of LAL, deposition of top mirror, and buckling of the top mirror.

scale mirrors [33], further enhancing cavity interactions, resulting in efficient photon extraction even when background emission is larger than the photon loss [34].

1.3 Monolithic and open-access FPC fabrication

Monolithic fabrication of FPCs leads to scalable, rapid, and consistent devices. In order to use these devices as FPCs for cQED the cavity mode must be accessible while not substantially degrading the figures of merit. To ensure compatibility with existing clean-room technologies the fabrication process should ideally be in compliance with CMOS fabrication processes.

Controlled thin-film buckling, a unique procedure used to fabricate optical devices with stress-driven self-assembly, has been under development by Dr. DeCorby's lab since 2010 [35]. This procedure, as shown in Figure 1.4, was first used to develop hollow wave-guides [35, 36] followed by air-core micro-cavities [37, 38]. The applicability of these micro-cavities to cQED was first demonstrated with Ta_2O_5/SiO_2-based devices by Potts [39, 40], followed by a-Si/SiO_2-based devices by Bitarafan [5, 41]. Numerous studies have been published characterizing these devices including their mechanical [42], thermal [40], and optical properties [41]. A summary of these devices in previous work including fabrication materials, low-adhesion layer (LAL) pattern diameter, peak device height, and reported FOMs are shown in Table 1.1.

Table 1.1: Historical cavity results with FOM for comparison.

Author	Material	D_d [µm]	δ [µm]	$\mathcal{F}$	Q	V_m
T. Allen [38]	a-Si/SiO_2	400	10.49	3000	40000	
T. Allen [38]	a-Si/SiO_2	300	8.75	2600	31000	
T. Allen [38]	a-Si/SiO_2	250	7.47	3200	32000	
T. Allen [38]	a-Si/SiO_2	200	5.68	2700	21000	
C. Potts [39]	Ta_2O_5/SiO_2	300	10.2	2930		390
C. Potts [39]	Ta_2O_5/SiO_2	250	8.81	2670		255
C. Potts [39]	Ta_2O_5/SiO_2	200	6.93	3030		191
C. Potts [39]	Ta_2O_5/SiO_2	150	4.68	3370		89
C. Potts [39]	Ta_2O_5/SiO_2	100	2.67	3560		35
M.Bitarafan [5]	a-Si/SiO_2	100	3.2	1000*	4000	8.7*
M.Bitarafan [5]	a-Si/SiO_2	50	0.78	1800	1800	1.3

*Estimated from related data in the paper.

Such buckled cavities will be referred to as a "cavity device" or "buckled device" for the remainder of this thesis.

A severe limitation of this fabrication procedure is the resulting sealed device, which makes the insertion of a emitter impossible. It is possible to pattern the emitter onto or under the LAL prior to deposition of the top mirror [43]. However, this approach limits the emitters available for study as they must be compatible with CMOS technology and able to survive the thermal shock of buckling.

Previous attempts to create open-access devices include etching access-holes with focused ion beam (FIB) milling [40] and opening side access through intersecting wave-guides [41], as shown in Figure 1.5. The FIB milling technique requires individual device alignment and resulted in degraded optical properties. The intersecting wave-guides require that the emitter traverse the enclosed channel to reach the cavity. While this method is suitable for micro-fluidic applications it is not practical for use with emitters that could adhere to side-walls.

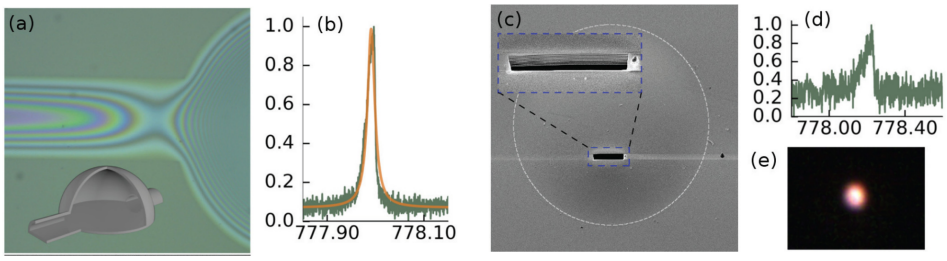

Figure 1.5: a) Microscope image of a FPC and the connected wave guide (with computer model of the device inset). b) Transmission spectra of the device shown in a). c) SEM image of a dome with a hole etched using FIB milling. d) Transmission spectra of the device shown in c). e) Fundamental mode of the device shown in c). Adapted from [40].

1.4 In this thesis

In this thesis, a novel monolithic fabrication procedure is described which etches access holes into pre-buckled devices, using reactive-ion etching (RIE) that is patterned through photolithography. The design, fabrication, and optical characterization of infrared range devices, and simulation of visible range devices is outlined. Preliminary fluid infiltration experiments were conducted to verify the open-access nature of the cavities. This procedure addresses the fabrication challenges outlined above while maintaining cavity FOMs.

Chapter 2 outlines the theoretical premises used to design and analyse the devices described in subsequent chapters. First, the basic resonance frequencies and finesse factors for the planar-mirror Fabry-Perot cavity are discussed. Next, the beam parameters such as minimum beam waist and resonant frequency of the fundamental mode of a spherical-mirror Fabry-Perot cavity, and the resonant conditions and mode profiles of higher order HG, LG, and IG modes are described. Theoretical parameters of distributed Bragg reflectors are then outlined, including design considerations such as reflectance and mirror penetration. Finally, key cavity-related FOMs used in this thesis including quality-factor (Q), mode-volume (V_{m}), and Purcell factor (F_{p}) are discussed.

Chapter 3 describes the design considerations and fabrication process for

the open-access buckled dome cavities. First, established fabrication procedures and device morphology are outlined, followed by the mask design considerations. Next, a detailed description of the device fabrication is given including mirror characterization and machine parameters. Finally, we discuss the morphological study used to select devices for further optical study. The result of this work is a monolithic process for fabricating large-scale arrays of high quality curved-mirror Fabry-Perot microcavities on a chip, with open access to the cavity regions. We verified that the incorporation of access holes using a dry etching process did not significantly impact the morphological or optical properties of the cavities.

Chapter 4 discusses the 'open access' optical results, consisting of optical analysis of monolithically fabricated open access devices compared to control devices on the same wafer. First, the experimental set-up used to measure the optical properties is described. Next, three representative devices are optically analysed including expected and extracted values of Q, V_{m}, and F_{p}. Finally, the fluid infiltration is described and confirmed. We demonstrated that liquid solvents could be introduced into the cavity, producing predictable changes to the optical and spectral characteristics of the HG/LG modes. While the proof-of-concept work employed 1550 nm-range mirrors, we see no significant barrier to replicating this work using our previously reported [40] buckled cavities operating in the visible and near-infrared region. This would expand the range of possible applications, and is an interesting topic for future work.

Chapter 5 presents our theoretical study of a-Si:H-based Bragg mirrors over Ta_2O_5-based mirrors for FPCs in the sub-micron range. We establish a theoretical model for the complex index of refraction after a thorough literature review. Then representative matrix simulations were performed both for the mirror characterization and for the emission rate of a dipole placed inside the planar FPC equivalent of the buckled-cavity. Finally a FDTD simulation

(using Lumerical) was performed to verify the matrix simulations. The predicted Purcell factor and cooperativity for both the matrix simulations and FDTD simulations are given.

Chapter 6 summarizes each chapter of this thesis, followed by future work suggestions.

Chapter 2

Optical cavity theoretical background

This chapter outlines the theoretical premises used to design and analyse the devices described in subsequent chapters.

2.1 Planar mirror Fabry-Perot cavities

While there are many assumptions in the canonical planar Fabry-Perot cavity (FPC) theoretical model, such as perfectly planar and aligned mirrors, it is nonetheless employed as an archetypal model for practically all other resonator types [44]. It should be noted that the following equations are based on the physical mirror spacing and are not exact for cavities with a length on the same order of magnitude as the wavelength. This discrepancy is due to a non-zero phase change on reflection and the non-negligible field penetration into the mirrors, which results in a variation in the cavity length, but the model nonetheless typically offers an adequate approximation [45]. Transverse modes are addressed in Section 2.2 in relation to spherical mirror cavities as transverse mode analysis isn't needed for a planar FPC and the following ray-optics based analysis is adequate.

In its most basic form, a planer FPC confines an electromagnetic field ($\vec{E}$) between two identical and perfectly parallel and planar dielectric mirrors (M_1,

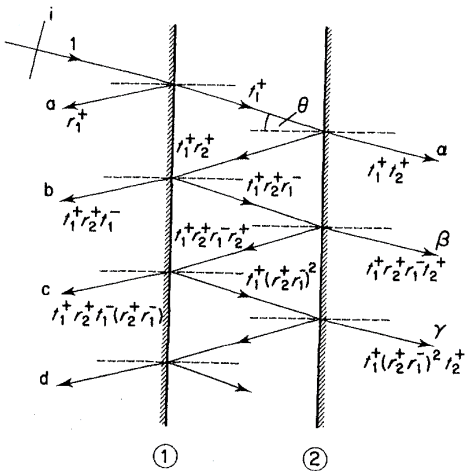

Figure 2.1: Basic FPC geometry, showing the progress of a single beam reflecting inside the cavity. The incident beam i is assumed to be of unity amplitude and also to be linearly polarized in either the parallel or perpendicular direction relative to the plane of incidence. The reflected beams are denoted with a, b, c, d and the transmitted beams are denoted with α, β, γ. The positive superscripts indicate the incident beam was travelling left to right, the negative superscript indicates that the beam was travelling right to left, with the subscripts indicating at which mirror the interaction occurred. Adapted from [44].

M_2), which are spaced at a some cavity length (L) apart, and with the cavity filled by some material with index of refraction n (*e.g.* air n ∼1 or IPA n ∼1.37). Each mirror has a reflectance (R), transmittance (T), absorption (A), and therefore potential transmittance(T_P), which can be calculated using the standard Fresnel equations or using transfer matrices for a multilayer mirror. In the simplest case, both mirrors are assumed to have 'hard-mirror' boundary conditions.

The basic ray analysis as shown in Figure 2.1 considers an incident electromagnetic plane wave with frequency ν and corresponding wavelength λ . It enters the cavity from the left through M_1 toward M_2 at an input angle of θ_i, here assumed to be normal to the cavity. Once the electromagnetic wave completes one round trip (*i.e.* travelled to M_2 and returned to M_1) the wave

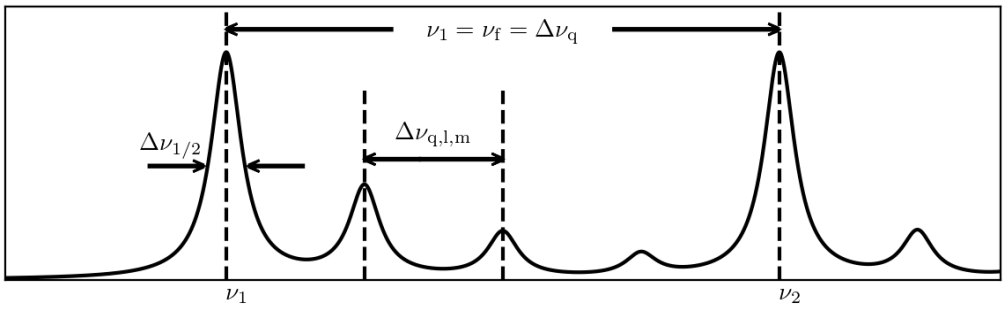

Figure 2.2: Example transmitted irradiance of a FPC *vs*. incident light frequency. Labelled are the free-spectral-range (ν_f), longitudinal mode spacing ($\Delta\nu_q$), the full-width half-max linewidth ($\Delta\nu_{1/2}$), and the higher-order mode spacing ($\Delta\nu_{q,l,m}$).

has undergone a phase shift of $\phi = 2L\frac{2n\pi}{\lambda}$ [44]. By summing the infinite number of sub-components which are circulating inside the cavity or transmitted through M_2, we can find the transmitted irradiance, where irradiance is defined as $I \equiv \frac{nc\epsilon_0}{2}\langle|\vec{E}|^2\rangle$, where ϵ_0 is the vacuum permittivity and c is the speed of light in a vacuum. If the input irradiance is of unity power per unit area, the transmitted irradiance is $I_t = (T_P)^2\,\mathcal{A}(\phi)$, where the Airy shape function is as follows:

$$\mathcal{A}(\phi) = \frac{1}{1 + K_F \sin^2(\phi/2)}. \tag{2.1}$$

Here, K_F is the coefficient of finesse [46], which depends only on the reflectance of the mirrors, given by $K_F \equiv 4R/(1-R)^2$.

The resonant condition is satisfied by those fields that maximize the transmitted irradiance, in other words, those which correspond to peaks in the Airy shape function. These are given by $\phi = 2\pi q$ where q is longitudinal mode order, a positive integer value. There are an infinite number of higher order longitudinal resonance frequencies given by $\nu_q = q\Delta\nu_q$ where the first non-trivial solution (*i.e.* $q = 1$) is $\nu_1 = c/2nL$. As shown in Figure 2.2, this not only corresponds to the fundamental longitudinal frequency (ν_1) but is also the longitudinal mode spacing ($\Delta\nu_q$) and the so-called free-spectral-range (ν_f),

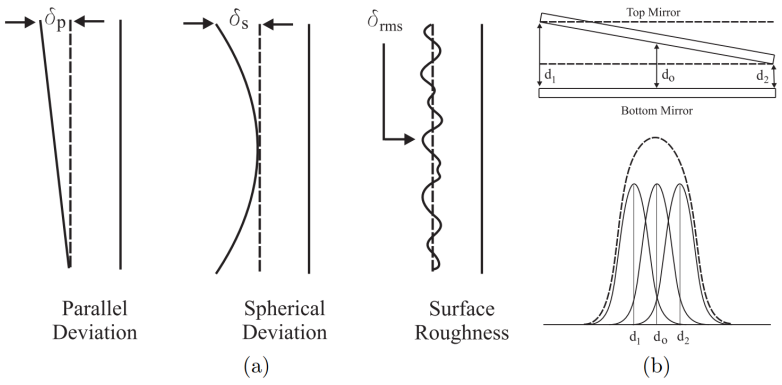

Figure 2.3: a) Various defects possible in FPCs. b) The effect of non-parallelism on a cavity. Adapted from [47].

the frequency range over which a FPC can be tuned.

For near-resonant conditions of the fundamental frequency, the transmitted irradiance can be approximated using the Lorentzian lineshape function [48], whose width is a measure of finesse. For high-finesse cavities this is given by $\mathcal{F}_{\text{eff}} = \nu_{\text{f}}/\Delta\nu_{1/2}$, where $\Delta\nu_{1/2}$ is the full-width at half-maximum linewidth. In the absence of other factors that cause photon loss (*i.e.* surface scattering, alignment issues), an ideal FPC has reflectance limited finesse $\mathcal{F}_{\text{R}} = \pi\sqrt{K_{\text{F}}}/2$. In reality, the effective finesse of the cavity is lowered by defect factors such as badly aligned mirrors, rough mirror surface, or spherical deviations [47]. This is illustrated in Figure 2.3 and quantified by the defect finesse ($\mathcal{F}_{\text{D}}$) where the effective finesse is then given by $\mathcal{F}_{\text{eff}} = \left(\frac{1}{\mathcal{F}_{\text{R}}^2} + \frac{1}{\mathcal{F}_{\text{D}}^2}\right)^{-1/2}$ [49].

2.2 Spherical mirror Fabry-Perot cavities

Realistic cavities do not adhere to the idealistic requirements for the planar FPC model, and in practice, planar cavities experience significant issues, including walk-off due to non-parallelism and surface-roughness [50]. By imposing boundaries in the transverse direction for the electromagnetic wave, the available modes in the cavity [51, 52] can be modified. This is typically done by curving one or both mirrors, thereby confining the fields inside the cavity.

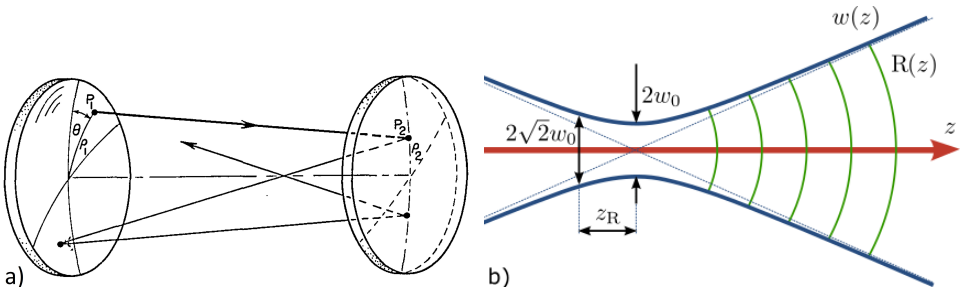

Figure 2.4: Basic spherical FPC geometry. a) shows a perspective of 3D spherical mirrors with a bounded ray retracing itself. Adapted from [53]. b) Gaussian beam parameters with an exaggerated beam showing the minimum beam waist, beam waist, Rayleigh range, and radius of curvature along the optical axis. Adapted from [54].

This can be viewed as a retracing of the beam path [53] as shown in Figure 2.4 a).

The simplest non-trivial solution to Maxwell's equations in spherical cavities is a beam with a Gaussian distribution across the transverse profile [55], which is a solution of the Maxwell's equations in the paraxial approximation (*i.e.* the Helmholtz equation) [48]. This Gaussian beam assumes a small divergence in the z direction and is cylindrically symmetric with the energy of the beam confined near the optical axis as in Figure 2.4b). The beam has the following irradiance profile with a radial coordinate ρ:

$$I(\rho, z) = I_0 \frac{w_0}{w(z)} \exp\left[\frac{-2\rho^2}{w(z)}\right]. \tag{2.2}$$

Here, w_0 is the minimum beam waist and $w(z)$ is the beam waist, defined as the radial coordinate where the intensity of the irradiance drops by $1/e^2$. The axially dependent beam waist can be expressed in terms of the minimum beam waist and the Rayleigh range (z_R):

$$w(z) = w_0 \left[1 + \left(\frac{z}{z_R}\right)^2\right]^{1/2}. \tag{2.3}$$

The Rayleigh range is the axial coordinate where the area of the beam is double that at the waist, given by $z_R = \pi w_0^2 n/\lambda$. This and the minimum beam waist

are often used interchangeably as a beam parameter, which can fully describe a first-order transverse electromagnetic mode (TEM) of a spherical mirror cavity.

Just as there are higher order longitudinal modes, there are also higher order transverse modes. To satisfy the boundary conditions of the Helmholtz equation and the phase conditions for constructive interference in a spherical-mirror optical cavity, the radius of curvature of the beam must equal the radius of curvature of the cavity mirrors. The radius of curvature of a Gaussian beam wavefront is given as follows:

$$\mathrm{R}(z) = z\left[1 + \left(\frac{z_\mathrm{R}}{z}\right)^2\right]. \tag{2.4}$$

This radius of curvature is impacted by Gouy phase, given by the so-called $\zeta(z)= \tan^{-1}(z/z_\mathrm{R})$. This describes the fact that the field near the center of the beam advances at a phase velocity that is greater than for a plane wave at the same frequency.

In the paraxial approximation, the higher order modes of the cavity are very nearly TEM and we can refer to them using two mode numbers: $\mathrm{TEM}_{\mathrm{l,m}}$. Three sets of transverse mode solutions are often discussed and examples of these sets are shown in Figure 2.5. All three mode sets acquire the Gouy phase similarly and are degenerate in highly symmetric cavities.

The first set are the so-called Hermite-Gaussian (HG) which are the natural solutions in Cartesian coordinates, by separating x and y modes of order l and m, respectively [59]. Defining the wavenumber as $k = 2\pi n/\lambda$, and denoting the Hermite polynomial of order x with H_x, the HG can be expressed as follows:

$$\begin{aligned} E_{\mathrm{l,m}}(x,y,z) = E_0 \frac{w_0}{w(z)} H_\mathrm{l}\left(\sqrt{2}\frac{x}{w(z)}\right) H_\mathrm{m}\left(\sqrt{2}\frac{y}{w(z)}\right) \exp\left[-\frac{x^2+y^2}{w(z)^2}\right] \\ \times \exp\left[-ik\frac{x^2+y^2}{2\mathrm{R}(z)} - ikz\right] \exp\left[i(l+m+1)\zeta(z)\right]. \end{aligned} \tag{2.5}$$

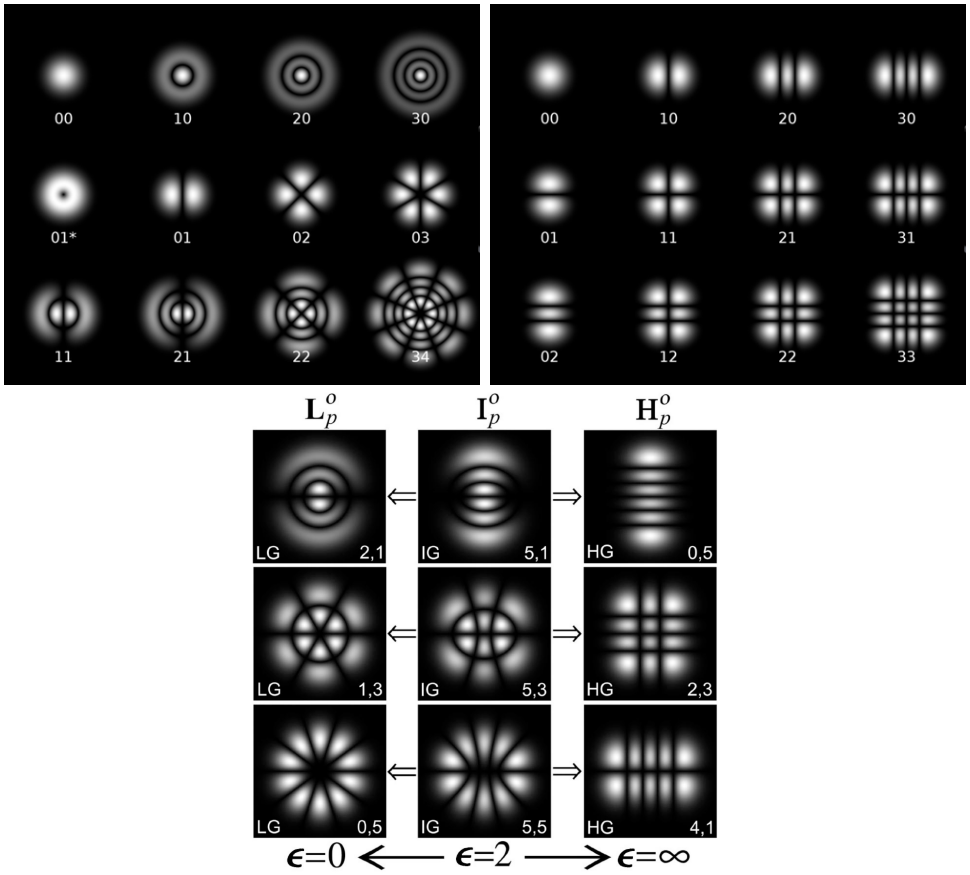

Figure 2.5: The top row shows the theoretical Laguerre-Gaussian (left panel) and Hermite-Gaussian resonant modes (right panel). The bottom panel shows the connection between IG, HG and LG modes. Adapted from [56–58].

For the HG modes, it can be shown:

$$\nu_{\mathrm{q,l,m}} = q\nu_{\mathrm{f}} + (l + m + 1)\frac{\Delta\zeta}{\pi}\nu_{\mathrm{f}}. \tag{2.6}$$

Here, $\Delta\zeta$ is the difference in the phase of the beam at either mirror, given by $\Delta\zeta = \zeta(z_2) - \zeta(z_1)$ where M_1 is at z_1 and M_2 is at z_2. In our half-symmetric buckled cavities, z_1 is set to coincide with the bottom planar mirror and therefore $\zeta(z_1) = 0$. It should be noted that even for $\mathrm{TEM}_{0,0}$ there is a non-zero frequency shift relative to the planar FPC case.

From the HG modes we can also determine the frequency separation of the higher order modes. In a half-symmetric cavity where the cavity length is much smaller than the radius of curvature of the spherical mirror, the mode

spacing is approximately given as follows:

$$\Delta\nu_{\mathrm{q,l,m}} \approx \frac{c}{2\pi n z_{\mathrm{R}}}\Delta(l+m). \tag{2.7}$$

The second set of higher-order modes are the Laguerre-Gaussian (LG) modes which are the natural solutions in cylindrical coordinates, separating the radial (ρ) and azimuthal (ϑ) coordinates for modes of order p and g, respectively [60]. The electric field is described as follows, where L_x^y is the Generalized Laguerre polynomial of order (x, y):

$$\begin{aligned} E_{\mathrm{p,g}}(\rho,\vartheta,z) = E_0\frac{w_0}{w(z)}\left(\frac{\sqrt{2}\rho}{w(z)}\right)^{|g|} L_p^{|g|}\left(\frac{2\rho^2}{w(z)^2}\right)\exp\left[-\frac{\rho^2}{w(z)^2}\right] \\ \times\exp\left[-ik\frac{\rho^2}{2\mathrm{R}(z)} - ikz + ig\vartheta\right]\exp\left[i(2p+|g|+1)\zeta(z)\right]. \end{aligned} \tag{2.8}$$

A third set are the Ince-Gaussian (IG) modes, which are superpositions of HG modes and LG modes [58] where the HG modes and LG modes are degenerate when $l+m = 2p+g$. These modes are connected by the ellipticity parameter ϵ, where HG modes are a special case with $\epsilon = 0$, and LG modes are a special case where $\epsilon = \infty$, as illustrated in Figure 2.5.

2.3 Distributed Bragg reflectors

Since the invention of the FPC, mirror technology has changed significantly. Metal mirrors are limited in their reflectance. For example, even perfectly polished gold mirrors are limited to R <0.997 [61] in the 700 nm to 2000 nm range which imposes a significant limitation, even for cavities with reflectance limited finesse. The introduction of dielectric thin films allowed for much higher quality mirrors through exploitation of interference effects. The reflectance of any thin film stack is determined by the complex indices of refraction, the film thicknesses, and the sequence of layers in the stack. Theoretically, there are no limitations on number of layers in a thin film stack and therefore the re-

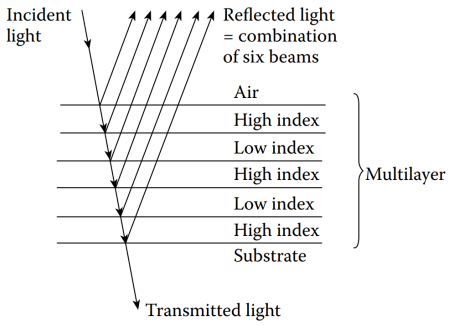

Figure 2.6: Bragg reflector mechanics, showing a 3.5 layer Bragg mirror. Adapted from [61].

flectance achieved. However, practical considerations such as deposition time and thin film quality impose limitations.

Dielectric thin film mirrors are variably called distributed Bragg reflectors (DBRs), 1D photonic crystals (PCs), or quarter-wave stacks (QWSs), depending on their exact design or their envisioned applications. Notably, DBRs with a reflectance of 99.9999 % have been fabricated [62]. The design of a high-reflectance periodic coating at a specific wavelength (λ_{B}) employs a stack of alternating high-index (n_{h}) and low-index (n_{l}) layers of corresponding thicknesses d_{h} and d_{l}. The optimal thickness of the constituent films is determined by the well-known quarter-wave condition:

$$\lambda_{\mathrm{B}} = 4n_{\mathrm{h}}d_{\mathrm{h}} = 4n_{\mathrm{l}}d_{\mathrm{l}}. \tag{2.9}$$

A DBR functions by creating destructive interference in the transmission direction while creating constructive interference in the reflected direction as shown in Figure 2.6. The primary determinants of the mirror reflectance are the layer quality (*i.e.* residual optical loss due to absorption and scattering) and the number of layers (N_{B}) [63]. The reflectance from a DBR can be estimated using the following equation where n_0 is index of refraction of input medium and n_{s} is index of refraction of substrate medium:

$$R_{\mathrm{B}} = \frac{n_0 n_{\mathrm{l}}^{2N_{\mathrm{B}}} - n_{\mathrm{s}} n_{\mathrm{h}}^{2N_{\mathrm{B}}}}{n_0 n_{\mathrm{l}}^{2N_{\mathrm{B}}} + n_{\mathrm{s}} n_{\mathrm{h}}^{2N_{\mathrm{B}}}}. \tag{2.10}$$

To achieve the high-reflection required for a FPC, the materials used for the mirrors must be chosen carefully. Specifically, the index contrast between the layers and their absorption coefficients largely determine the mirror properties. The extinction coefficients of the layers determines the maximum reflectance and the potential transmission. The T_{P} is the probability that a non-reflected photon is transmitted through the mirror, as opposed to being absorbed or scattered [64] and is defined as follows: $T_{\mathrm{P}} = T/(T + A)$. In many cases (*e.g.* see Chapter 5), this can be estimated by neglecting loss in the low-index layers and determining the limiting absorptance due to loss in the high-index layers.

A large index contrast (Δn) between the materials positively influences several cavity parameters. The index contrast determines the width of the stop-band, the field penetration into the mirror, and the number of periods required to achieve a certain reflectance [65], as in Equation 2.10. At normal incidence, the range of reflected wavelengths (*i.e.* the stop-band width) can be estimated as follows:

$$\Delta\lambda_{\mathrm{B}} = \lambda_{\mathrm{B}} \frac{4}{\pi} \sin^{-1} \frac{\Delta n}{n_{\mathrm{h}} + n_{\mathrm{l}}}. \tag{2.11}$$

The field penetration depth can be estimated as:

$$\delta_{\mathrm{p}} = \frac{\lambda_{\mathrm{B}}}{4n'\Delta n} \tag{2.12}$$

in a DBR with a large Δn, where $n' = (n_{\mathrm{h}} d_{\mathrm{h}} + n_{\mathrm{l}} d_{\mathrm{l}})/(d_{\mathrm{h}} + d_{\mathrm{l}})$.

2.4 Figures of merit for optical cavities

Three primary figures of merit will be used to quantify the cavity devices. The first two are classical FOMs derived from Maxwell's equations, specifically the quality-factor and mode-volume [66–68], whereas the third is the Purcell factor, which requires cavity quantum electrodynamics to fully understand its meaning.

The quality-factor of a FPC is a measure of how well the cavity contains the resonant energy temporally, and is often used as a measure of resolving power. A universal definition of Q (often used for electrical resonance circuits and microwave resonators) is as follows:

$$Q = 2\pi \left(\frac{\text{stored energy}}{\text{energy loss per cycle}} \right). \tag{2.13}$$

An equivalent and more useful definition of the quality-factor (appropriate if the cavity is of high quality) is $Q = \frac{\nu_q}{\Delta\nu_{1/2}} = q\mathcal{F}_{\text{eff}}$. This can be measured experimentally using spectral scans similar to Figure 2.2. It can be theoretically predicted using the estimated longitudinal mode number and the reflection-limited finesse.

The second FOM (technically, figure of demerit, but nevertheless) is the mode volume, often expressed in units of λ^3 where λ is the mode wavelength in the cavity. The mode-volume of a FPC is a measure of how well the cavity contains the resonant energy spatially, and cavities with a small mode-volume are generally desirable. Our buckled devices are half-symmetric cavities with a planar mirror on the bottom and an approximately spherical mirror on top.

For our half-symmetric cavities [69] with E_0 as the peak value of the electric field in the cavity, the mode-volume can be estimated as:

$$V_m = \frac{\iiint_{V_c} \epsilon_0 |\vec{E}|^2 dV}{\epsilon_0 E_0^2} \approx \frac{\pi}{4} w_0^2 L_{\text{eff}}. \tag{2.14}$$

Here, w_0 is the mode waist radius at the flat mirror and L_{eff} is the effective cavity length. The effective cavity length is the length of the cavity plus the penetration into both mirrors (*i.e.* $L_{\text{eff}} = \delta + 2\delta_p$). The minimum beam waist in our cavities can be approximated as [23]:

$$w_0 \approx \sqrt{\frac{\lambda}{\pi}} (L_{\text{eff}} \cdot R_{oc})^{1/4}, \tag{2.15}$$

with R_{oc} being the effective radius of curvature of the curved (buckled) mirror. The extracted estimates of mode-volume were calculated using similar spec-

tral scans as the quality-factor, and by determining the effective cavity length from the fundamental frequency and the radius of curvature. The mode volume can be extracted from experimental measurements of the transverse mode separation and using Equation 2.7 to find the Rayleigh range followed by Equation 2.4 to find the radius of curvature. The mode volume can alternatively be predicted using the morphology of the cavity devices, as will be described in subsection 3.1.1, where elastic buckling theory provides an equation for the effective radius of curvature based on device height.

The final FOM quantifies the cavity enhancement of the spontaneous emission into a cavity mode of interest (γ_c) over the free space emission (γ_0). This enhancement is highly dependent on the alignment between the emitter and the cavity, with the maximum possible enhancement attained for an emitter that is perfectly aligned (spatially, spectrally, and in terms of polarization) to the cavity mode of interest. This ideal enhancement is known as the Purcell factor and is expressed as [70]:

$$F_p \equiv \frac{\gamma_c}{\gamma_0} = \frac{3}{4\pi^2}\frac{Q_{eff}}{V_m/\lambda^3}. \tag{2.16}$$

If the emitter has a narrow linewidth, as assumed here, we can approximate $Q_{eff} \sim Q$. Therefore, the ideal Purcell factor can be determined from the mode-volume and quality-factor alone.

A high F_p requires a high quality-factor and a low mode-volume, which historically has been difficult to achieve simultaneously. From the Purcell factor, some other useful FOMs can be derived, including the cooperativity and the photon coupling efficiency.

Reducing V_m requires limiting several parameters including the maximum buckle deflection(δ), mirror penetration (δ_p), and effective radius of curvature (R_{oc}) of the buckled mirror. These goals are addressed with short cavity lengths that are inherent to the buckle structures, high-index contrast mate-

rials limiting the penetration depth, and devices with small dome radii [41].

High Q in macroscopically aligned classical FPCs is achieved by increasing the cavity length, which raises the longitudinal mode order. However, increasing the length of the cavity also increases the mode-volume, and as such it is typically desirable to maximize the finesse of the cavity. The two limiting factors of finesse are $\mathcal{F}_{\mathrm{R}}$ due to the mirror reflectivity, and $\mathcal{F}_{\mathrm{D}}$ due to defect factors. To maximize the cavity finesse we aim to have a reflectance-limited finesse in our cavities and, historically, our buckled dome FPCs have achieved nearly reflection-limited finesse due to the monolithic and self-assembly-driven nature of our fabrication process.

Chapter 3

Fabrication of single-wafer open-access Fabry-Perot micro-cavities[1]

This chapter describes the design considerations and fabrication process for the open-access buckled dome cavities. First, the established fabrication procedure and device morphology is outlined and then the mask design for these devices is described. Next, a detailed description of the device fabrication is given including mirror characterization and machine parameters. Finally, the morphological study of the devices is over-viewed to help in the device candidate selection for optical scans.

3.1 Design considerations and fabrication procedure

The baseline fabrication procedure has been described previously [41] but is summarized briefly as follows (see Figure 3.1):

1. The bottom distributed Bragg reflector (DBR) (4-period SiO_2/a-Si quarter-wave stack, nominally centered at 1550 nm wavelength) is deposited using an RF magnetron sputtering system.

[1] A version of this chapter was published in *Applied Optics*, vol. 59, no. 23, pp. 7125-7130, 2020.

2. A low-adhesion layer (LAL), which is a 'Teflon-like' fluorocarbon film, is deposited using the Bosch-process passivation-cycle in a deep-reactive-ion-etch (DRIE) chamber and patterned using a lift-off procedure.

3. The top DBR (4 periods) is deposited using the same RF magnetron sputtering system, following parameters that result in a desired amount of compressive stress.

4. The wafer is subjected to a heating step (<400 °C), releasing the top mirror over the patterned LAL regions resulting in buckled delamination. When the patterned LAL regions are circles, the buckled features form half-symmetric (plano-concave) Fabry-Perot microcavities with an enclosed 'air core'.

We explored two fabrication strategies and from these attempts it was determined that the buckling step must precede etching (the first unsuccessful method is outlined in Appendix B.2) and therefore we must etch the already-buckled device, either from the front (*i.e.* top surface of the wafer) or the back. While etching from the back could have potentially interesting applications, we chose to etch from the front, as the top mirror is significantly thinner than the bottom mirror and substrate combined.

The fabrication process shown in Figure 3.1 was selected and is briefly described as follows. First, the photo resist (PR) is spun-cast onto the pre-buckled devices and patterned using photolithography prior to etching. A reactive-ion etching (RIE) procedure was chosen for a number of reasons including its high etch-directionality (independent of crystal orientation), fidelity in pattern transfer, and compatibility with CMOS technologies [71]. In order to control etch parameters such as etch rate, profile, and selectivity (between Si, SiO_2, and PR), a chlorine-based chemistry was used [72].

It was difficult to determine the thickness of the PR film due to the flat

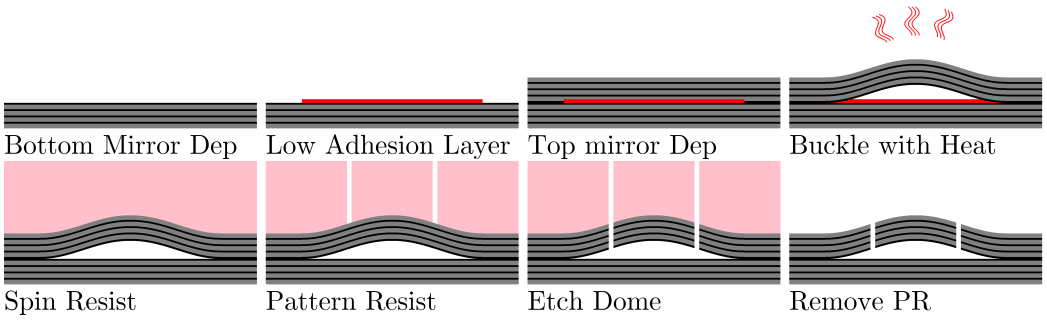

Figure 3.1: New fabrication process, in which access holes are etched into pre-buckled domes. The dimensions are not to scale and the process is depicted from top left to bottom right. The top row is a copy of Figure 1.4 which depicts the existing process. Subsequently, the PR is spun-cast and patterned, the top mirror is etched using RIE, and finally the PR is removed using an acetone bath.

surface (regardless of device height) that arises from the PR spin-casting. A ∼10 µm-thick PR film was used to ensure that none of the devices were damaged during the etching process.

3.1.1 Device morphology

As described above, the buckled dome cavities are formed 'spontaneously' due to the compressive stress of the upper mirror. This mirror can be treated as a thin plate with an effective-medium elastic-modulus and stiffness [19]. It has been demonstrated (*e.g.* see Refs. [19, 42]) that devices fabricated using the buckling procedure adhere to elastic buckling theory [73]. Ideally, the RIE procedure would not modify the buckled-device's profile, however, this was an open question at the outset of this research project.

Previous work has shown that buckling only occurs if the diameter of the LAL is larger than the critical diameter (*i.e.* $D_\mathrm{d} > D_\mathrm{min}$) or if the internal compressive stress of the film is larger than the critical stress (*i.e.* $\sigma > \sigma_\mathrm{c}$), given by:

$$\sigma_\mathrm{c} = 1.2235 \frac{E}{1-v^2} \left(\frac{d}{D_\mathrm{d}/2} \right)^2 . \tag{3.1}$$

This depends on several film parameters including Young's modulus (E), Pois-

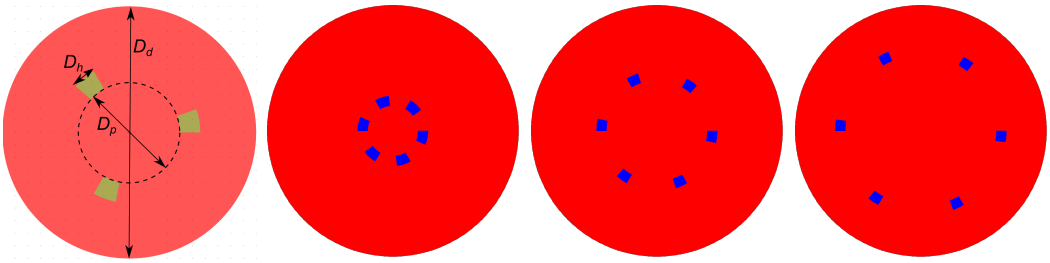

Figure 3.2: Mask pattern of a 3-hole buckled device. Red signifies the LAL and green or blue indicate the etch pattern. Three device configuration parameters are indicated on the far left device: D_p, D_h, and D_d. The remaining three images show representative D_p configurations.

son's ratio (v), and film thickness (d).

If we assume purely elastic deformation (*i.e.* ignoring plastic deformation) we can then find the deviation profile from the wafer surface (Δ) by treating the delaminated mirror section as a clamped circular plate. The predicted shape in this case is described by the Bessel function of order zero and first kind (J_0) whose first zero occurs for an argument of μ=3.8317, as follows [73]:

$$\Delta(\rho) \approx \delta\left[0.2871 + 0.7129 J_0(\mu\rho)\right]. \tag{3.2}$$

Here, δ is the maximum height of the circular buckled structure given by $\delta = \max(\Delta(\rho)) = d\left[1.9\left(\sigma/\sigma_\mathrm{c} - 1\right)\right]^{1/2}$ [74] and ρ is the radial coordinate normalized to the dome radius (*i.e.* $D_\mathrm{d}/2$). From this, we can determine the minimum radius of curvature at the top of the buckled devices, as follows:

$$\mathrm{R_{oc}}(0) = \mathrm{R_{oc}} = \frac{2}{0.7129\delta}\left(\frac{\mathrm{D_d}/2}{\mu}\right)^2 \tag{3.3}$$

This radius of curvature allows us to estimate the anticipated minimum beam waist and therefore the higher-order mode spacing. This is used to calculate the predicted mode-volume in Chapter 4.

3.1.2 Mask Design

We speculated that etching holes into the upper mirror might modify the geometrical and optical properties of the domes, and that the number, loca-

tion, and size of the etch holes might play an important role in this regard. Additional alignment issues could arise if the etched holes were too close to the center of the device, as they might then coincide with the optical mode. Conversely, if the holes were etched too close to the LAL-boundary, inadequate clearance between the top and bottom mirrors might make open-access impossible and could invalidate the boundary conditions in elastic-buckling theory.

To investigate these potential effects, a mask with varying device sizes and etch hole configurations was implemented. We varied four device parameters: dome-base diameter (D_d), etch-hole pattern diameter (D_p), etch-hole size (D_h), and the number of holes (N_h), as shown in the left image of Figure 3.2. In all cases, the etch holes were symmetrically distributed on the circumference of a circle, nominally concentric with the dome. The pattern diameters were chosen to be larger than the region spanned by the low-order optical modes [41].

Domes with base diameters of 50 µm and 100 µm were successfully fabricated and etched. Etch pattern diameters were one of $D_\mathrm{p} = 0.2D_\mathrm{d}$, $0.4D_\mathrm{d}$, or $0.6D_\mathrm{d}$ as shown in Figure 3.2, and etch hole sizes were either 3 µm, 4 µm, or 5 µm.

The mask is divided into cells, each of which contains 512 devices evenly distributed between eight different patterns of increasing invasiveness, with N_h of 0, 3, 4, 5, 6, 8, 10 or 12. The effect of each of these device parameters is described at the end of this chapter.

3.2 Fabrication details

First a DBR was deposited onto a new and cleaned silicon wafer. The 4-period a-Si/SiO_2 Bragg mirror was deposited using a reactive magnetron sputtering system with identical targets of 0.99999-pure n-type Si for both materials. A

Table 3.1: RF magnetron sputtering parameters for a-Si and SiO_2

Material	Power [W]	Frequency [kHz]	Duty Cycle [%]	O_2 flow [SCCM]	Chamber Pressure [mTorr]
a-Si	200	150	92.5	NA	3
SiO_2	200	150	88	3.2	4

base chamber pressure of $<1 \times 10^{-6}$ Torr was maintained and the substrate was held at 150 °C with Ar flow of 50 SCCM into the chamber for the deposition of both materials. A test deposition for each material was performed using the parameters described above and those in Table 3.1. The test films were subsequently scanned with a variable-angle spectroscopic ellipsometer (VASE), which revealed an index of refraction of $n_{\mathrm{h}} \approx 3.7$ and $n_{\mathrm{l}} \approx 1.46$ for a-Si and SiO_2, respectively, and an extinction coefficient of $\kappa_{\mathrm{h}} < 1 \times 10^{-2}$ and $\kappa_{\mathrm{l}} < 2.8 \times 10^{-3}$ at 1550 nm for a-Si and SiO_2, respectively. The DBRs were centred at 1550 nm, resulting in a quarter-wave stack (QWS) with a thickness of $d_{\mathrm{h}} \sim 116$ nm and $d_{\mathrm{l}} \sim 283$ nm. The film data was confirmed with the VASE measurement of the bottom mirror, as seen in Figure 3.3 and compared to the results from a transfer matrix simulation of a DBR [75]. The simulation and the VASE results show $R > 0.99$ across the range from 1400 nm to 1700 nm. A profile SEM image of the top mirror is also shown, clearly revealing the darker a-Si and lighter SiO_2 layers. The stress of this QWS was measured using the 'Flexus Wafer Stress Measurement system' and was found to have a compressive stress of ~ -180 MPa, similar to values reported by our group previously and adequate to initiate buckling.

The LAL used for these devices is a 'Teflon-like' layer that is deposited using the sidewall passivation cycle of an inductively coupled plasma reactive ion-etching (ICPRIE) machine 'Alcatel AMS110', typically used for the Bosch etching process [76]. The LAL is patterned through lift-off using PR HPR 504, in turn spun-cast using a standard nanoFAB recipe that results in a PR layer

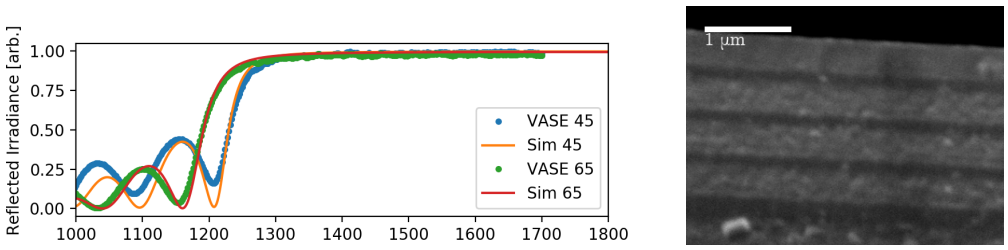

Figure 3.3: Left: Reflected irradiance of the bottom mirror measured using VASE and compared to the simulated reflectance from a 4-period a-Si/SiO_2 mirror with the properties discussed in the text. Right: A SEM image taken at an angle where the top mirror has been cleaved such that the 4 periods of a-Si and SiO_2 are visible. Where the top mirror adheres to the bottom mirror can be seen in the double-thick layer at the bottom.

$\sim$1 µm thick.

Next, a top mirror was deposited in the same conditions as the initial bottom mirror described above. In our usual process, the wafer is then diced to allow for buckling of smaller pieces, which has typically resulted in a higher yield of high quality devices in past work in our lab. However, as described above, here the whole wafer was buckled at once since our wafer needs to be etched after buckling. The wafer was placed on a hot plate under a microscope for visual monitoring and was initially heated to $\sim$100 °C. From there, the temperature was slowly increased by 50 °C/ min until buckling was observed, typically at $\sim$350 °C.

The access holes were patterned using MicroChemical's AZ P4620 Resist (AZ P4620) due to its ability to be spun-cast to the desired thickness mentioned above. First the PR (AZ P4620) was applied to the wafer via spin coating using the CEE 200CB Coat Bake System. The standard recipe calls for a series of steps that requiring multiple hours to complete. Therefore, our lab developed a modified recipe that can be completed in an afternoon. First the PR is spun for 10 s at 500 RPM followed by a 25 s spin at 2000 RPM. The wafer is then baked twice at 100 °C for 90 s and left to rehydrate for 10 min between baking steps. This results in a PR layer approximately 10 µm thick,

Table 3.2: Sputtering parameters for the 'Teflon-like' LAL using Alcatel AMS110

Coil Power [W]	C_4F_8 flow [SCCM]	Chamber pressure [mTorr]	Chuck temperature [°C]	Chuck bias [V]	Chuck position [mm]
600	60	5	10	0	120

which we found to be suitable for patterning holes with critical dimensions of approximately 4 µm.

Next the PR is patterned using a broadband-UV source mask-aligner with a CCD alignment system (specifically the system labelled as Bert in the nanoFAB). This alignment system allows for manipulation in both transverse directions, the adjustment of the relative angle between the wafer and the mask, and the ability to align two locations at once on the wafer through two CCD monitors. The alignment step was done manually and without full contact between the wafer and the mask. This is necessary due to the small amount of translation possible while the wafer is making contact with the mask. In the future, the use of an automatic alignment system could likely result in improved and more consistent results. After photoresist patterning, the wafer was diced, and chips were attached to a carrier wafer using crystal bond or wafer tape for the subsequent etching process.

We etched holes by RIE using the Cobra Reactive Etch system from Oxford Instruments at the nanoFAB facility. This RIE system uses inductively-coupled plasma to increase the bombardment while avoiding damage to the substrate. This is an automated system, allowing us a great amount of control over the etching conditions. The parameters used to etch the a-Si and SiO_2 mirrors are listed in Table 3.3. After RIE, the remaining PR was removed using an acetone bath. It is worth noting that attempts to use the Branson 3000 Barrel Etcher or the oxide burn in the COBRA machine to remove PR were not succesful and the remaining PR was extremely difficult to remove.

Table 3.3: Etching parameters for the Cobra Reactive Etch system

Wafer RF [W]	ICP RF [W]	Chamber Pressure [mTorr]	Wafer Temperature [°C]	$CHF_3/SF_6/O_2$/ Ar flow [SCCM]
300	1000	90	20	50/ 10/ 0/ 25

This process flow resulted in successful devices with open access as seen in Figure 3.4. Devices with 3 µm holes were not etched, likely due to incomplete exposure of the thick photoresist for such small-scale features. Devices with 4 µm and 5 µm holes were reliably etched and produced similar results. It was noted that some buckled devices with D_h of 4 µm exhibited inconsistent etching; this was likely due to inconsistencies in the PR patterning [77] around the buckled domes and chemical transport limitations during RIE of small features, since this was not observed in the larger trench areas.

It is worth noting that the etch holes were typically almost circular on the wafer, in contrast to those on the mask design which are defined as straight-sided arc-sections. This can be attributed to the the partially isotropic nature of the dry etch and the limited resolution for defining µm-scale features in the thick photoresist. Circular etch holes may actually be preferable, since they do not create sharp corners that could act as nucleation sites for cracking.

3.3 Fabricated device morphology

To analyse the effect of the etched holes on the device morphology, over 2000 ZYGO NewView 5000 optical profilometer (ZYGO) scans were performed, each generating a surface map of the device. From this surface map, the profile of the devices (centred at the device peak (δ)) consisting of aggregated data for all radial directions was generated. In the surface plots, anomalous points around the etched holes appeared; these were likely due to ZYGO's inability to resolve the near vertical walls of the etched holes. This was confirmed by

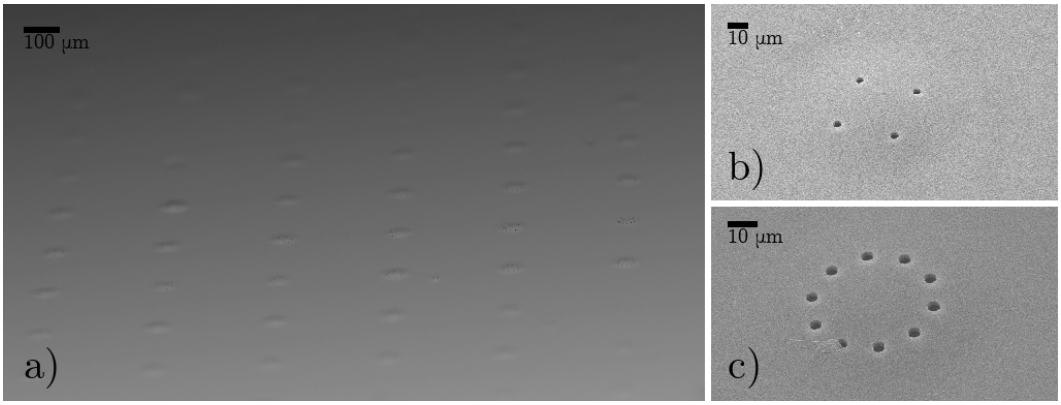

Figure 3.4: Many buckled domes with etch holes. a) shows multiple adjacent domes successfully etched and buckled b) shows a dome with 4 etch holes, c) shows a dome with 12 etch holes.

imaging a device around the etch holes and these anomalous points were observed in neither microscope, nor scanning electron microscope (SEM) images. The surface map was centred using a Hough transform [78] to detect the circular device. The peak height of the buckled devices was found by assuming the peak to be inside the etched region (thereby avoiding the anomalous data).

Each device discussed in this subsection is represented with two images, the first showing a three-dimensional plot and the second showing a flattened profile view. The three-dimensional plot contains a surface map with gradient shading of the ZYGO scan and contour maps normalized to the device height projected behind and below. The second plot shows the aggregated profile, described above, compared to the predicted profile from elastic buckling theory (Δ), and the estimated hole location is drawn in dashed lines (assuming ideal alignment). This visualization method gives an indication of the cylindrical symmetry of the devices and can be used to determine if the devices deviate significantly from the predicted profile.

As discussed in subsection 3.1.2, there are four design parameters that were varied in this study: D_{d}, D_{p}, D_{h}, and N_{h}. The implications of D_{d}, D_{p}, and D_{h} are discussed below and those of N_{h} are discussed in the next chapter.

Three sets of buckled-devices were analysed visually for cylindrical symmetry and agreement to elastic buckling theory. The first set investigates the affect of dome-base diameter and hole diameter, and relevant data is shown in Figure 3.5. The second set investigates the affect of pattern diameter of $0.2D_{\mathrm{d}}$ and $0.6D_{\mathrm{d}}$, and the corresponding data is shown Figure 3.6. The last set, with data plotted in Figure 3.7, shows a control device without etch holes compared to a representative device with the configuration selected for subsequent optical study.

First, the dome diameter and etch hole diameter were considered to determine the effect of the relative and absolute etch hole size on the buckled devices. Both representative devices have a medium etch pattern (*i.e.* D_{p}=$0.4D_{\mathrm{d}}$). Here, the device diameter is only considered insofar as open-access is concerned, since the effect of dome diameter on device properties has been covered extensively in previous work (*e.g.* see Table 1.1). Most devices with D_{d} of 50 µm showed weak (but consistent) buckling (δ∼0.5 µm and a yield of 88 %) and therefore did not support any modes in the 1550-nm wavelength range of interest. A representative device with a D_{d} of 50 µm, D_{h} of 4 µm, and a N_{h} of 3 is shown in Figure 3.5 (a). This was the least invasive etch pattern that resulted in open-access devices, however, a notable deviation from the predicted profile was seen. This implies a possible deviation for very small mode-volume devices (*i.e.* those with minimum height and radius of curvature) similar to those described previously [41]; however, this was not investigated in detail here and a full study is left for future work.

Devices with D_{d} of 100 µm showed consistent buckling and many devices had resonant frequencies within the range of our tunable laser (*e.g.* δ∼1.8 µm with a yield of 91 %). A representative device with D_{d} of 100 µm, D_{h} of 5 µm, and a N_{h} of 6 is shown in Figure 3.5 (b). This device had the largest etch holes and very little deviation was observed in similar devices with N_{h}

below 4. However, similar devices degraded rapidly as N_{h} increased, whereas devices with a D_{h} of 4 µm showed a lower level of degradation across all hole configurations. A full study of the impact of etch hole size is left to future work. In the subsequent analyses we focus on devices with D_{h} of 4 µm.

Next, the effect of the pattern size was considered with two representative devices shown in Figure 3.6. Due to the sensitivity of Fabry-Perot cavities to mirror deformations (*i.e.* deviations from the spherical shape), the most invasive etch patterns (*i.e.* N_{h} of 12) are expected to maximize any effects on the device profile. First, a representative device with the tightest pattern ($D_{\mathrm{p}} = 0.2D_{\mathrm{d}}$) is shown with significant deviation from the predicted profile. This is possibly due to the closer proximity of the holes to one other or their proximity to the peak of the device, thereby modifying some assumptions of the predicted profile. Next, Figure 3.6 b) shows a device with the widest pattern ($D_{\mathrm{p}} = 0.6D_{\mathrm{d}}$) which also shows a deviation from the theoretical model. It is possible this is due to the removal of material near the edges, which could violate the assumptions of the clamped plate elastic buckling theory. As will be shown, the medium pattern ($D_{\mathrm{p}} = 0.4D_{\mathrm{d}}$) was found to have little effect on the dome morphology, and we focus the remainder of the discussion that follows on devices from this group.

In contrast to the previous two sets of devices, the set in Figure 3.7 shows devices with a high level of cylindrical symmetry (however, see the comments below) and agreement with elastic buckling theory. The first device shows a control device (*i.e.* $N_{\mathrm{h}} = 0$) which agrees with previously reported devices and was fabricated on the same wafer as the other devices discussed. This second device shows the most invasive pattern (*i.e.* N_{h} of 12) of the preferred device configuration: D_{d} of 100 µm, D_{p} of 40 µm, D_{h} of 4 µm. All devices with this configuration showed a high level of symmetry (*e.g.* see Figure 4.2 in the next chapter) and were subsequently optically characterized.

From the generated profiles of preferentially configured devices it was found that, regardless of the circular symmetry of the etched holes, most buckled devices retained good circular symmetry. This indicates that the etching of small holes through the domes did not significantly modify the overall stiffness and mechanical rigidity of the upper-mirror buckled 'plate'.

It is notable that an increasing number of etch holes (as shown in Chapter 4) or an increase in etch hole size tended to cause increasing deviations from cylindrical symmetry. This might be due to some circumferential 'rippling' in the buckle shape caused by the dense pattern of holes, but might also be caused in part by variations in the fabrication parameters. For example, the size of individual etch holes was observed to vary even on individual domes, due to the challenges associated with patterning small features in thick photoresist, mentioned above. For a given application, fluid dynamics considerations will likely also play a role in determining the optimal number and size of the access holes. A more complete study of these details is left for future work.

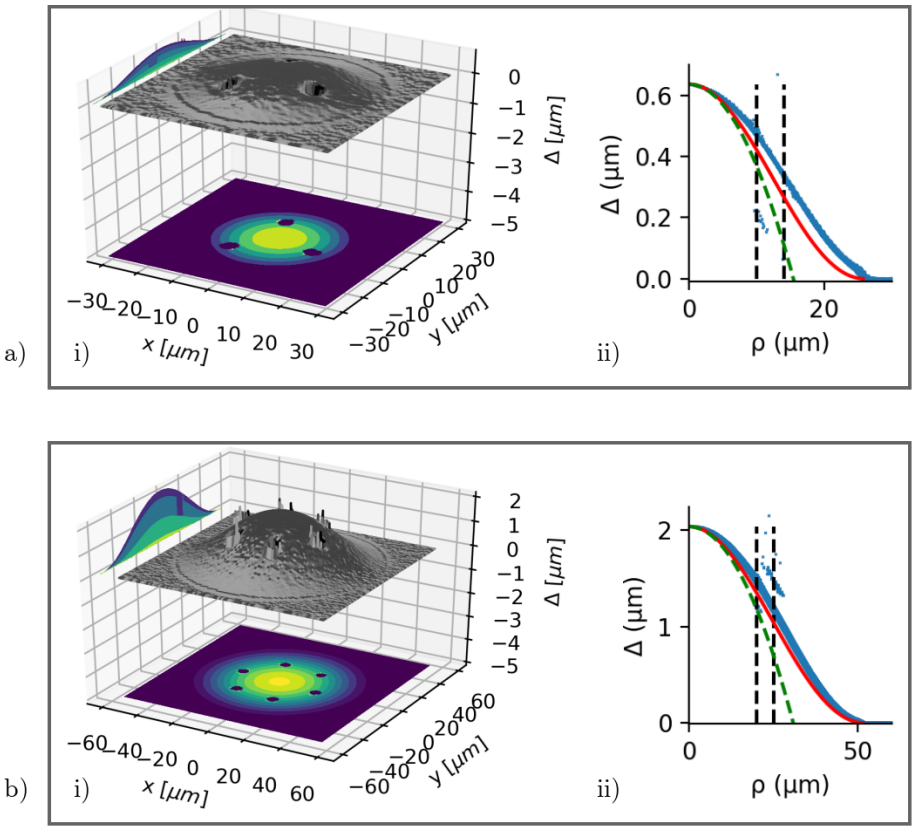

Figure 3.5: Two representative devices showing the effect of the etched hole size on the buckled device morphology. a) is a buckled device with D_{d} of50 µm, D_{p} of 20 µm, D_{h} of 4 µm, and N_{h} of 3. b) is a buckled device with D_{d} of100 µm, D_{p} of 40 µm, D_{h} of 5 µm, and N_{h} of 6. Deviations from the predicted profile is shown in both devices. Each row contains the data for one device, where i) shows a surface plot with gradient shading of the ZYGO scan and contour maps, normalized to the device height, projected behind and below. ii) shows the same aggregated, overlaid data for all radial directions extracted from profilometer scan in blue, the predicted buckled profile in red, the predicted profile of spherical dome with the effective radius of curvature at the top of the buckle is shown in green, the black bars indicate where the etch holes are patterned in ideally aligned devices.

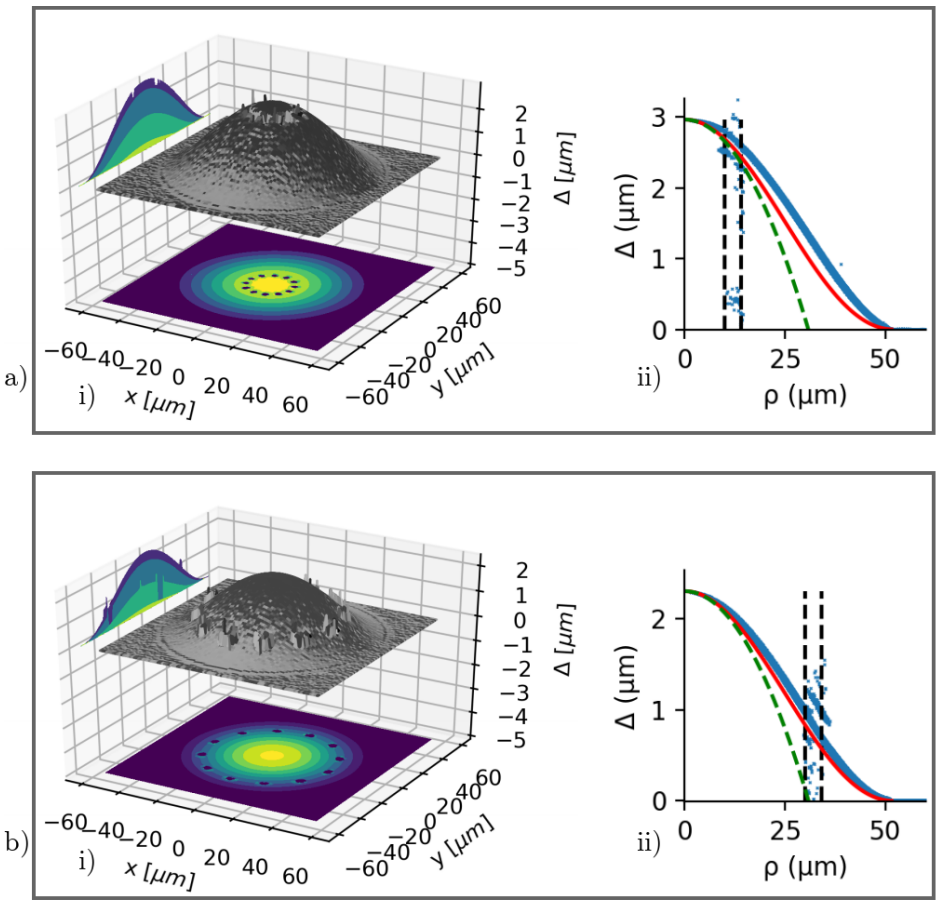

Figure 3.6: The same morphological visualizations as described in Figure 3.5 Two representative devices showing the effect of the pattern size on the buckled device morphology. a) is a buckled device with D_{d} of 100 µm, D_{p} of 20 µm, D_{h} of 4 µm, and N_{h} of 12. b) is a buckled device with D_{d} of 100 µm, D_{p} of 60 µm, D_{h} of 4 µm, and N_{h} of 12. Deviations from the predicted profile were observed in both devices.

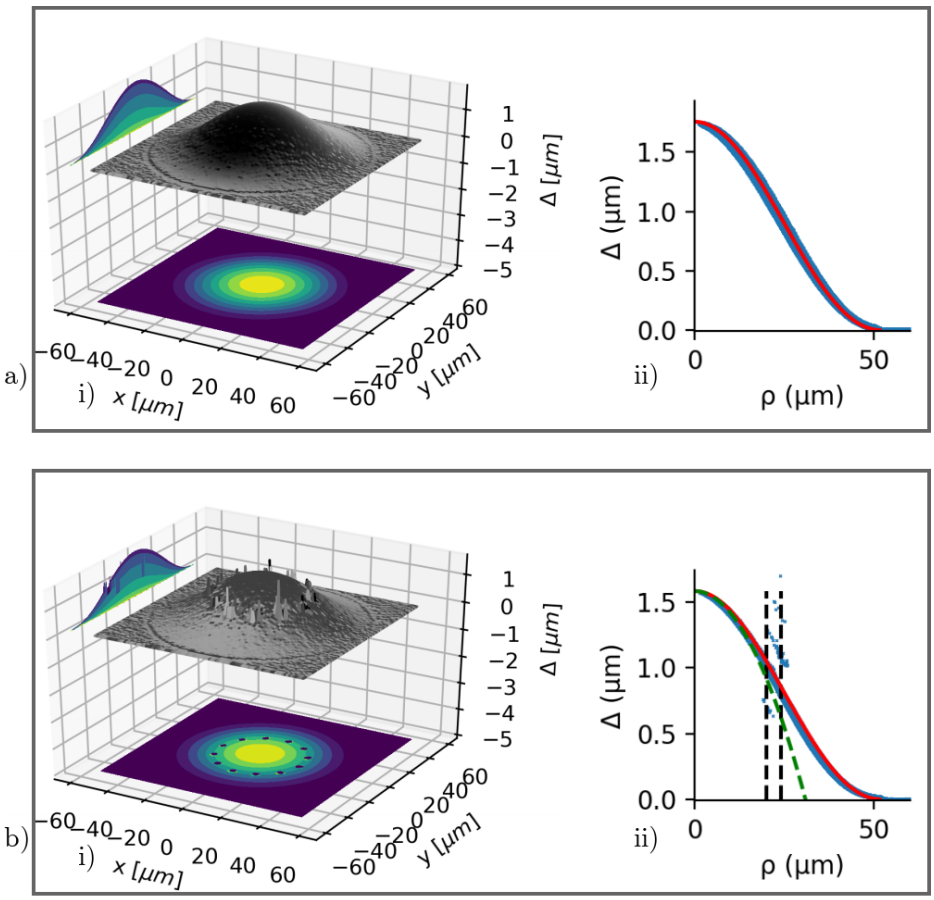

Figure 3.7: The same morphological visualizations as described in Figure 3.5. Two representative devices showing the affect of the etch hole size on the buckled device morphology. a) is a buckled device with D_{d} of 100 µm and no etch holes used as a control. b) is a buckled device with D_{d} of 100 µm, D_{p} of 40 µm, D_{h} of 4 µm, and N_{h} of 12. Relatively small deviations from the predicted profile were observed in both devices.

Chapter 4

Optical characterization of open-access Fabry-Perot micro-cavities[1]

The chapter discusses the 'open access' project optical results, consisting of optical analysis of monolithically fabricated open access devices compared to control devices on the same wafer. First the experimental setup used to measure the optical properties is described. Next, three representative devices are optically analysed providing estimations of Q, V_{m}, and F_{p}. Finally, the fluid infiltration of select domes is described and confirmed.

4.1 Optical microscope experimental set-up

Spectral measurements were performed in a custom optical microscope setup, using a tunable laser (Santec TSL 710) as an excitation source and an infrared camera (Raptor Ninox) as a photo detector. The vertical optical path encompassed a parabolic-mirror-based fiber collimator, a focusing objective lens, a sample translation stage, variable-power objective lenses on a rotating turret to collect the light transmitted through the cavities, and a tube assembly incorporating lenses, beam splitters, and/or filters. The tunable laser was coupled

[1] A version of this chapter was published in *Applied Optics*, vol. 59, no. 23, pp. 7125-7130, 2020.

to the back of the devices and could be tuned between 1480 nm and 1620 nm in wavelength. This experimental arrangement is shown in Figure 4.1, with the insets showing the beam splitter and the objective arrangement around the sample in closer detail.

First the laser beam is focused and aligned with the camera; this is done either with a large amount of attenuation or with a plain silicon wafer in the optical path. The laser beam was focused so the spot size was minimized on the wafer and centred in the camera. The sample was then placed on the stage so that the relevant cell aligned with the through-hole, with some clearance for laser focusing. The sample was then brought into the laser path, and the relevant device was aligned to the focused laser spot. If a fundamental mode was found from a coarse scan, a higher-power objective was selected for more detailed observation. The center of the device was aligned by maximizing the intensity of the transmitted mode in the center of the device. The camera was used in place of a photo diode to ensure the transmission measurements did not include the light leaking through the etched holes. The transmitted irradiance was calculated from a select area of the camera, set to include the area of the optical modes inside the etch hole pattern. The camera settings were constant during the scans with maximum intensity and the pixel integration time adjusted to stay below saturation.

4.2 Cavity Device Characterization

Spectral scans were taken of all the devices described in this section as well as representative devices of the configurations described in Section 3.3. Most devices which showed a deviation from the expected profile (as described previously) exhibited a lowered quality-factor and therefore a lower predicted Purcell factor. However, the tight pattern (*i.e.* $D_\mathrm{p} = 0.2D_\mathrm{d}$) could be of interest as the extracted quality-factor was *larger* than the predicted value in most

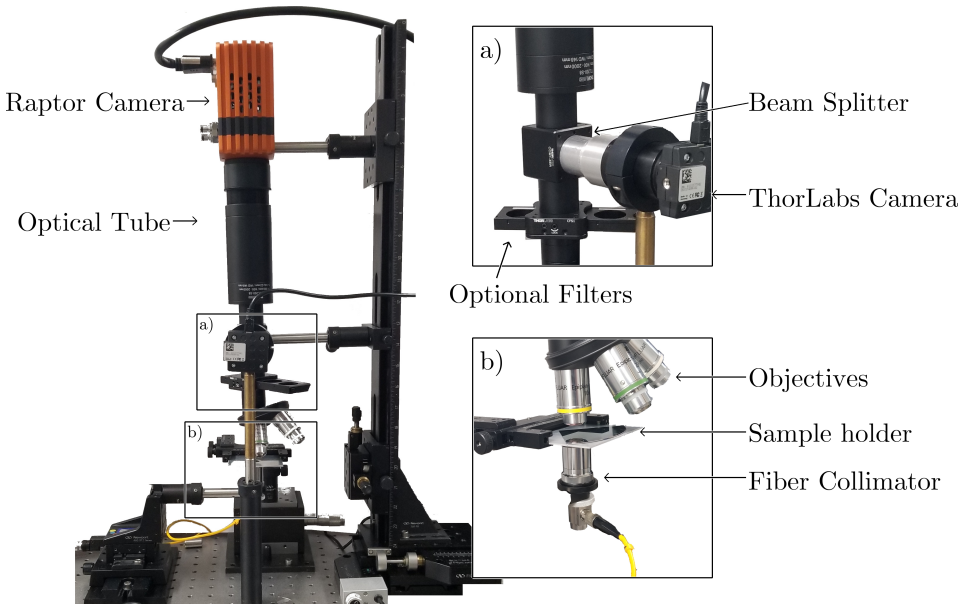

Figure 4.1: Experimental spectral set-up. The insets show more detail of the junction points on the set-up with relevant labels.

devices scanned, up to a factor of 146 %, while the V_{m} was not affected. This unexpected observation of a cavity enhancement was not studied in detail in this thesis project and is left for future work. All the devices discussed below have the preferred device configuration (D_{d} of 100 µm, D_{p} of 40 µm, D_{h} of 4 µm mentioned in Section 3.3), similar peak heights, and are from an area within a 3 mm by 3 mm square in the same cell on the wafer. Within such a small area on the wafer, it is reasonable to assume that all devices have a similar etch hole alignment, mirror properties, and fabrication properties.

The measurement of each characterized cavity device consisted of an optical profilometer scan, two spectroscopic scans using the optical microscope set-up described above, and images taken from the microscope setup using a CMOS camera. The ZYGO scan provides the peak device height (δ) as described in Chapter 3, which can be used to predict cavity figure of merit (FOM) values using the theory outlined in Chapter 2. The fundamental frequency (ν_{q}) and the full-width at half-maximum linewidth ($\Delta\nu_{1/2}$) were measured using a high-resolution optical scan performed using the above-described optical

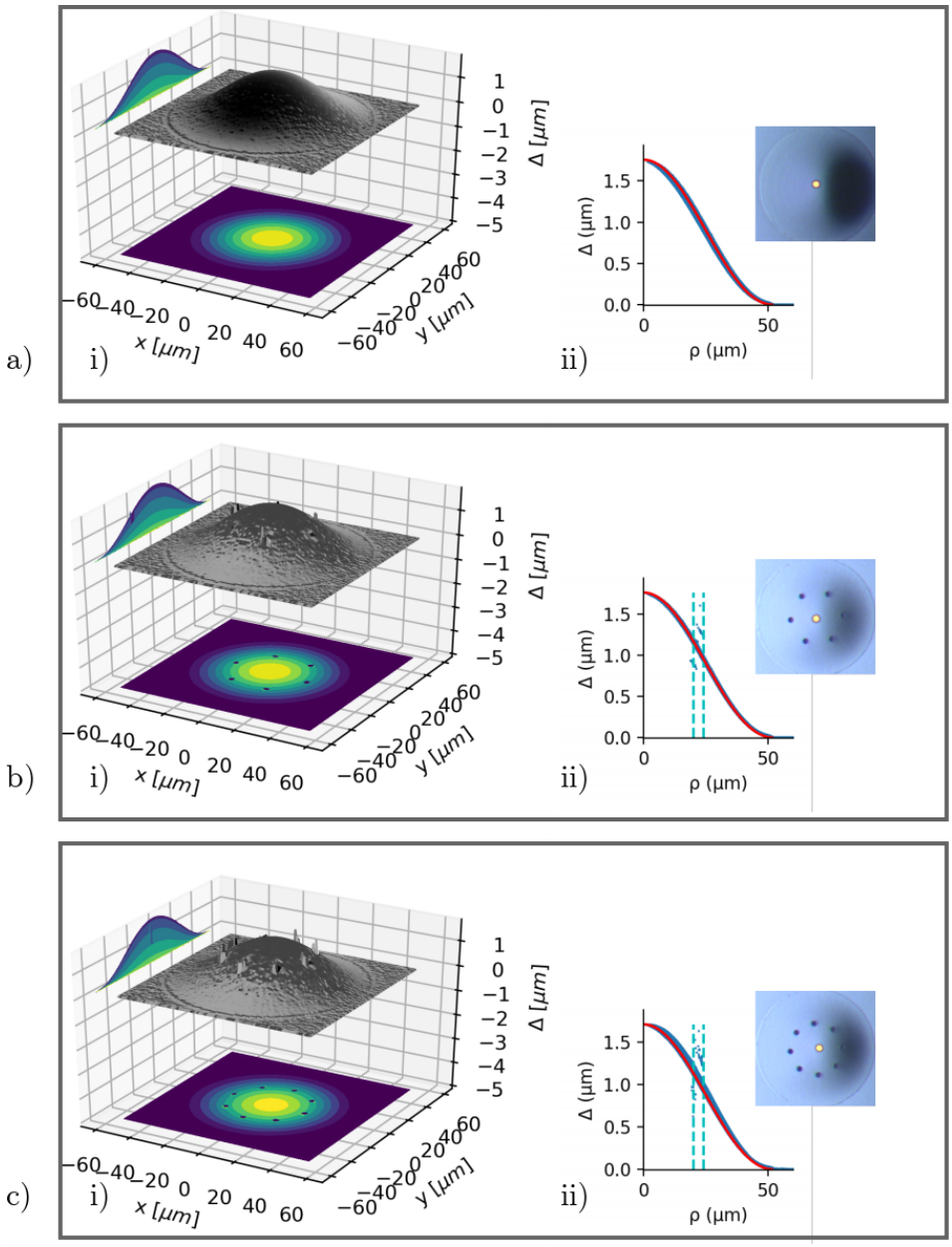

Figure 4.2: The same morphological visualizations as described in Figure 3.5 except for ii) a removal of the circular fit plots and the addition of a CMOS camera image showing the device with the fundamental mode superimposed, showing the mode location in the dome relative to the etched holes. Three representative devices to illustrate the affect of the number of holes on the buckled device morphology. a) is a buckled device with D_{d} of 100 µm and no etch holes used as a control. b) is a buckled device with D_{d} of 100 µm, D_{p} of 40 µm, D_{h} of 4 µm, and N_{h} of 6. c) is a buckled device with D_{d} of 100 µm, D_{p} of 40 µm, D_{h} of 4 µm, and N_{h} of 8. Only slight deviations from the predicted profile were observed in any of these devices.

Table 4.1: Extracted data from the spectral measurements for different hole configurations (N_h) on devices with D_d of 100 µm, D_p of 40 µm, and D_h of 4 µm.

	ZYGO	Extracted spectral measurements		
N_h	δ [µm]	ν_q [THz]	$\Delta\nu_{1/2}$ [GHz]	$\Delta\nu_{\mathrm{q,l,m}}$ [THz]
00	1.76	186.1	41.3	1.7
03	1.75	186.6	41.9	1.7
04	1.77	185.9	46.0	1.7
05	1.77	185.2	49.5	1.6
06	1.76	187.2	35.1	1.6
08	1.71	194.1	58.4	1.6
10	1.75	188.5	53.0	1.6
12	1.75	188.6	50.7	1.6

microscope set-up with a resolution of 0.01 nm centred at the fundamental frequency. The spacing between higher order modes ($\Delta\nu_{\mathrm{q,l,m}}$) was estimated using a low-resolution optical scan performed with a resolution of 0.1 nm across the fundamental mode and at least five higher order modes. The measured values of all the N_h configurations are shown in Table 4.1.

The predicted values are calculated using the following from Chapter 3: morphological properties, peak device height (δ), and theoretically predicted mirror reflectance. The quality-factor is calculated by estimating the longitudinal mode number from the cavity height (*i.e.* q of 2 for all devices presented here) and assuming that our cavities are high quality with reflectance limited finesse (*i.e.* $Q \sim q\mathcal{F}_\mathrm{eff}$ and $\mathcal{F}_\mathrm{eff} \sim \pi\sqrt{K_\mathrm{F}}/2$). The mode-volume is calculated from the morphological data, the effective cavity length, and the minimum beam waist in Equation 2.14. The effective cavity length ($L_\mathrm{eff} = \delta + 2\delta_\mathrm{p}$) is calculated from the mirror data in Chapter 3 and the morphologically predicted radius of curvature is used with Equation 2.15 to estimate the minimum beam waist and therefore the mode-volume.

The extracted quality-factor is calculated using a high-resolution spectral scan to determine the fundamental frequency and the full-width at half-maximum linewidth. The extracted mode-volume is calculated using the fun-

damental frequency to estimate the effective cavity length and higher-order mode spacing to find the Rayleigh range by Equation 2.7 (and by extension the minimum beam waist). Both the predicted and extracted FOMs for all N_{h} configurations are shown in Table 4.2. It should be noted that there was a small yet consistent discrepancy between the predicted and calculated mode-volumes, possibly due to the FPC-length-based equations not holding exactly for cavities with a cavity length on the same order of magnitude as the wavelength. Nevertheless, the predicted and extracted mode-volume are in near agreement for all devices. The quality-factor however, generally decreases with increasing N_{h} and we speculate this is due to the etch holes causing cavity asymmetries, thus decreasing the defect finesse of the cavities.

The exact effect of varying numbers of holes is not entirely clear and is left to future study, but in order to provide a representative analysis, three devices are presented with their full morphological and spectral scans. The chosen devices were a control device with no etched holes, a device whose optical Q was relatively improved by the etching (*i.e.* N_{h} of 6), and a device whose optical Q was apparently degraded by the etching (*i.e.* N_{h} of 8). Morphological data is shown in Figure 4.2, where the visualization is the same as in the previous chapter with a microscope image and fundamental TEM mode inset in the profile plot. All the devices measured showed high levels of cylindrical symmetry and profiles in agreement with predictions of elastic buckling theory.

The mode images and spectral data for these devices is shown in Figure 4.3 with each row describing one device. Data shown includes: i) The $\mathrm{TEM}_{0,0}$ mode with the intensity profile and a Gaussian profile overlayed, ii) The fundamental mode from the high-resolution spectral scan with the Lorentzian profile overlayed, iii) The low-resolution spectral scan where the inset higher order TEM modes (up to the fifth order) were captures by the CMOS camera, and converted to a contour map normalized to the maximum irradiance. The

fundamental Gaussian mode of these devices are shown for each device and shows high agreement with the expected Gaussian profile. The high-resolution spectral scans for the control and the 6-hole device are similar, but the larger FWHM is clear in the 8-hole case. The full optical scans of all devices show clear modes, consistent mode spacing, and some amount of mode splitting. The estimated level of mode splitting can be seen in these longer scans, with the 8-hole device showing more mode splitting than the other devices. The insets show the transverse cavity modes, up to the fifth order. These are most likely IG or LG modes, indicating cylindrical symmetry that is slightly broken in all devices. This suggests more deviations from the theoretical profile in the 8-hole device, likely accountable for the lowered $\mathcal{F}_{\text{eff}}$ (and therefore lower Q and F_{p}).

The main conclusion drawn from this study was that the addition of the etch holes caused minimal change in the gross details of the cavity shape, across the range of parameters studied. Even with a relatively large number of holes, implying a relatively large amount of material removed from the top mirror, the high-level shape of the dome is still well-approximated by the profile predicted for a buckled uniform circular plate. We speculated that this can be attributed in part to the fact that the holes were etched after the 'plates' were buckled. Upon buckling, the compressive strain energy stored in a film is greatly reduced [79], so that the forces which might drive further reshaping of the buckled feature (*i.e.* after hole etching) are relatively small. A more complete study of the thermo-mechanical properties of the hole-modified domes, including modification of the effective spring constants and mechanical frequencies, could be an interesting topic for future work [19].

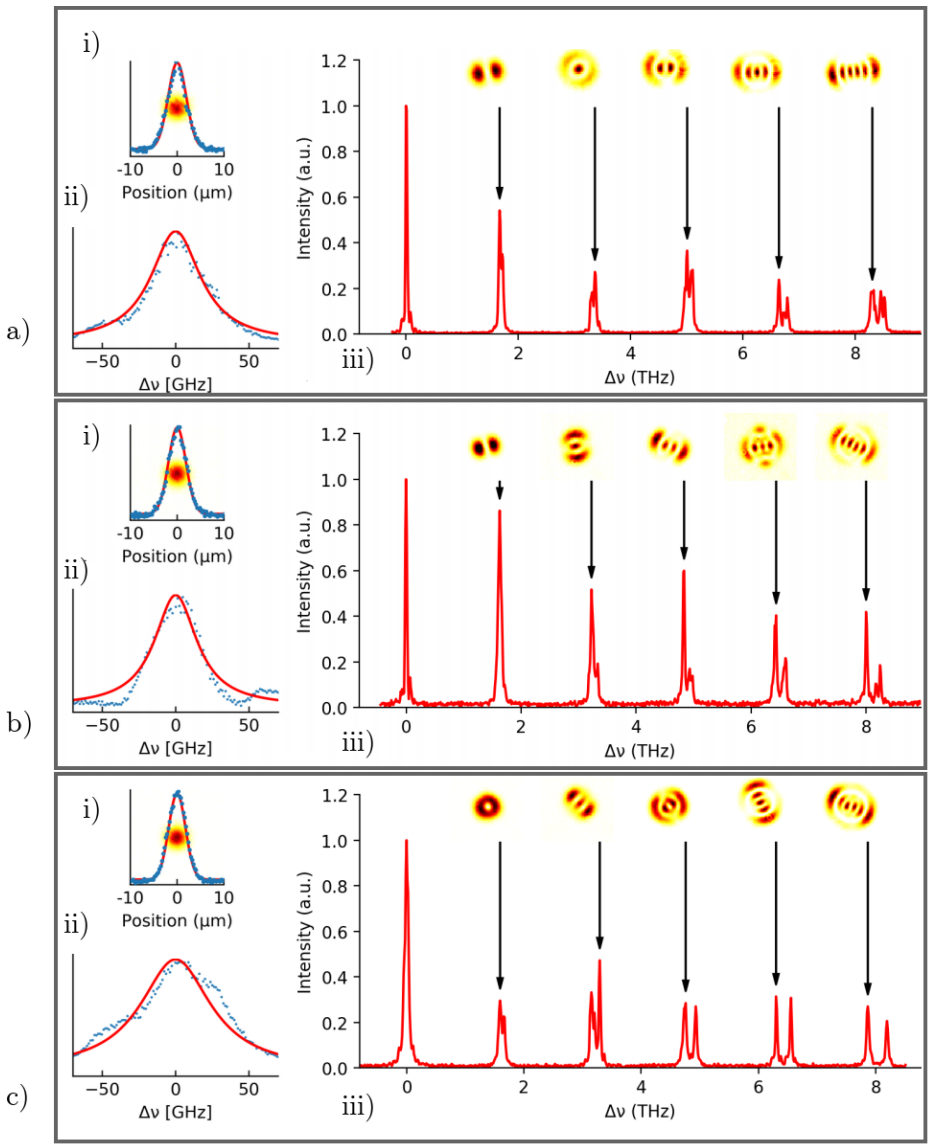

Figure 4.3: Spectral scans of devices with each row showing N_{h} of 0, 6 and 8 respectively. i) The $\mathrm{TEM}_{0,0}$ mode with the intensity profile and a Gaussian profile overlayed, ii) The fundamental mode from the high-resolution spectral scan with the Lorentzian profile overlayed, iii) The low-resolution spectral scan where the higher order TEM modes inset were taken with the CMOS camera and converted to a contour map normalized to the maximum irradiance up to the fifth order.

Table 4.2: Calculated data for different hole configurations (N_h) on devices with D_d of 100 µm, D_p of 40 µm, and D_h of 4 µm.

	Predicted			Extracted from spectral scans		
N_h	Q	V_m	F_p	Q	V_m	F_p
00	4700	4.8	75	4500	4.5	77
03	4700	4.8	75	4400	4.5	75
04	4700	4.8	76	4000	4.5	69
05	4700	4.7	76	3700	4.5	63
06	4700	4.8	75	5300	4.6	88
08	4700	4.9	73	3300	4.8	53
10	4700	4.8	75	3500	4.7	57
12	4700	4.8	75	3700	4.6	61

4.3 Optical scans of fluid-filled devices

Selective infiltration of the dome cavities is made challenging by their small size, and especially by the small size of the individual micro-pores. Future work could benefit from the addition of on-chip microfluidic channels or reservoirs [80, 81]. As a preliminary exercise, we used a micro-pipette (WPI, tapered glass with 1 µm inner diameter at the tip), attached to a micro-positioner and an automated pump (WPI PicoPump) to dispense small-volume droplets over individual dome cavities (see Figure 4.4(a)). Similar approaches have been widely employed for the study of liquids interacting with microcavities and waveguides [82–84]. While the volume of the 'empty' cavity region in the buckled domes is <1 pL, the smallest droplet volumes we were able to dispense with our pump setup were on the order of 10s of picoliters. Thus, each dispensed droplet was typically much larger than the target dome, as can be discerned from the images in Figure 4.4. Given this, an alternative approach might have been to 'flood' the chip surface with a larger volume of liquid. However, the use of the micropipette reduced the required amount of solvent and also facilitated real-time observations of changes in optical properties as liquid droplets advanced or receded in the vicinity of a particular cavity.

Initially, water was used but it did not penetrate into the domes when

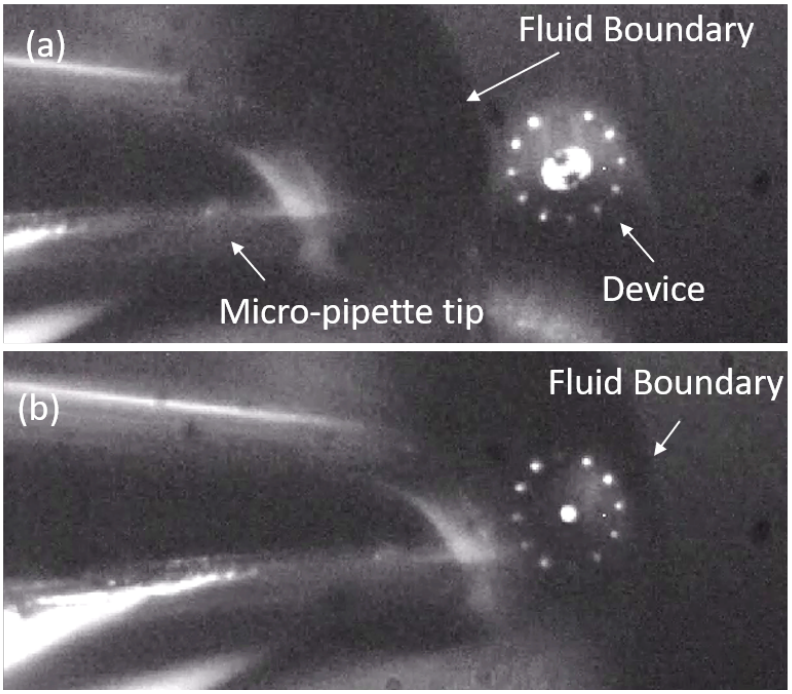

Figure 4.4: (a) Screen-shot image of a cavity just prior to infiltration by IPA. The laser frequency is fixed, and the cavity is resonating in a high-order transverse mode pattern. (b) Image captured after fluid infiltration, showing the cavity resonating in a fundamental mode. Sequential dispensing and evaporation of droplets caused repeatable transition between these two states. In both images, scattered light can be seen 'leaking' through many of the etch holes. Note that the laser is incident from beneath the sample, so that the images correspond to transmitted light collected by the camera.

deposited. We then tried hexane, which was successful however it evaporated very quickly. We then turned to isopropal alcohol (IPA), which is what was used for all the measurements discussed in this section.

First, note that for domes with no etch holes (*i.e.* $N_{\mathrm{h}} = 0$), we confirmed that dispensing IPA droplets onto the cavity had no discernible effect on the optical/spectral properties. This is expected, since the resonant light is highly confined between the mirrors of these cavities, and changes to the external medium (*i.e.* from air to IPA) does not significantly change the electromagnetic environment for the confined modes. On the other hand, dispensing droplets onto domes with etch holes produced dramatic and predictable

changes in the optical/spectral properties. For example, Figure 4.4(a) shows a screen capture of a particular dome with D_{d}=100 µm, $D_{\mathrm{p}} = 60$ µm, $D_{\mathrm{h}} = 4$ µm, and $N_{\mathrm{h}} = 12$, and with the micro-pipette aligned nearby but prior to dispensing liquid. The laser frequency is fixed, and from the camera image it is clear that the cavity is resonating in a high-order HG/LG/IG mode under these 'empty-state' conditions. Figure 4.4(b) is a second screen-shot captured less than a second later, after the fluid droplet has advanced over the cavity and infiltrated through the holes. Under these conditions, the cavity is supporting a fundamental mode – the laser was tuned to this condition after pre-scanning the cavity. We observed predictable transitions between two such states by repeatedly depositing a droplet of hexane on a similar cavity and letting it evaporate between each deposition. Once the devices were characterized while empty we deposited fluid into the domes.

A second example is shown in Figure 4.5. Here, we chose a smaller cavity (D_{d}= 50 µm, $D_{\mathrm{p}} = 10$ µm, $D_{\mathrm{h}} = 4$ µm, $N_{\mathrm{h}} = 5$) with peak height ∼0.55 µm, too short to support cavity modes in the 1550 nm range when the space between the mirrors is filled with air. This was confirmed by scanning the empty cavity, as evidenced by the image shown in Figure 4.5(c), for example. Note that the 5 bright spots in the image are due to light leakage through the bottom mirror and the etch holes of the top mirror, and are not associated with a cavity mode. Assuming IPA infiltrates and fills the cavity volume, the optical length of the cavity is expected to increase by a factor of ∼1.37 (*i.e.* to ∼750 nm). This is sufficiently large to support modes of fundamental longitudinal order at the probed wavelengths, as was confirmed both by the appearance of cavity modes (Figure 4.5(d)) and from spectral scans (Figure 4.5(a)-(b)) after IPA droplets were dispensed. Note that the scan in Figure 4.5(a)-(b) is noisier compared to the example shown in Figure 4.3. This is due in part to the use of a longer working distance (lower NA) objective to collect the output light

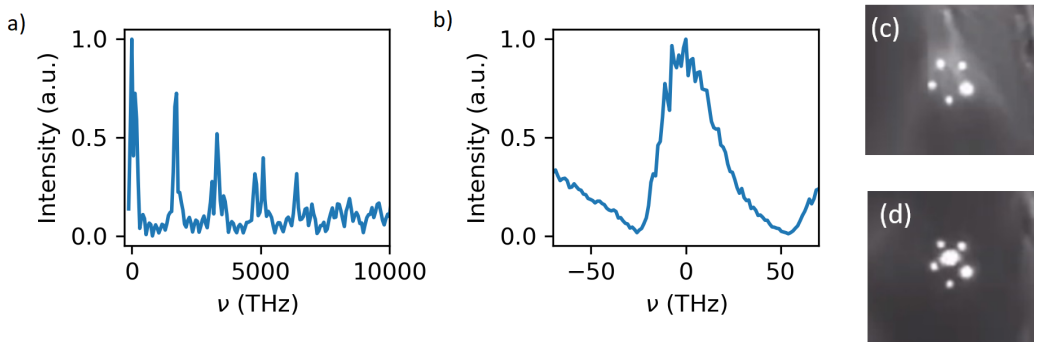

Figure 4.5: a),b) Show optical scans of the dome filled with IPA. c),d) Microscope images showing the small device filled (d) and empty (c)

here, in order to accommodate the micro-pipette tip.

A resonant mode is clearly visible, although the scans of the filled-fluid dome are noisier. This is due to the fast evaporation of the liquids used, and additional unpredictable reflections due to the liquid layer in and around the device, making it difficult to characterise the exact cavity parameters while full. We also identified several higher order modes in the device as well, as it acted similarly to any of the larger devices studied above. Without fluid inside the device the cavity is not long enough to support a mode. This with the optical scans described above proves conclusively that the devices described here are of high quality-factor, low mode-volume, and open access. Experimentation with emitters and other fluids are left to future work.

Chapter 5

Theoretical study of silicon-based Bragg mirrors for sub-micron cQED applications[1]

In this chapter we conducted a theoretical study on the potential use of amorphous hydrogenated silicon (a-Si:H) as the high index material in quarter-wave-stack Bragg mirrors for cavity QED applications. Compared to conventionally employed Ta_2O_5, a-Si:H provides a much higher index contrast with SiO_2, thus promising significantly reduced layer-number requirements and a smaller mode volume. Silicon-based mirrors offer the additional advantage of providing a wide omnidirectional reflection band, which allows greater control of the background electromagnetic modes. From numerical studies at 850 nm, we show that a-Si:H-based mirrors could enable significant improvements with respect to maximum Purcell factor, cooperativity, and spontaneous emission coupling factor, in addition to their potential to reduce fabrication complexity. These advantages are anticipated to be even more compelling at longer wavelengths.

[1] A version of this chapter has been submitted for publication.

5.1 Introduction

The cavity devices described in the previous two chapters are centered at 1550 nm, suitable for telecommunications applications [85] and is within the range of interest for some emitters. However, in cavity quantum electrodynamics (cQED) there is great interest in the <1000 nm range due to the traditional use of single alkali-atoms as emitters [86, 87]. Most work to date has employed Ta_2O_5/SiO_2-based mirrors, due to their typically excellent mechanical properties and ultra-low scattering and absorption losses for near-infrared operation, enabling reflectance as high as $R > 0.99999$[63] in extreme cases. Cavities with finesse exceeding 104 at 950 nm [24, 88] and 780 nm [23, 30] wavelengths have been reported, typically requiring 15-22 period mirrors. Recently, $\mathcal{F} > 5 \times 10^5$ was reported for a cavity operating at 1550 nm and employing 18-period mirrors [20]. Such mirrors are on the order of $\sim 8\,\mu$m thick and require a closely controlled, relatively expensive, and time consuming deposition process. Moreover, the relatively low index contrast between Ta_2O_5 ($n \sim 2.15$) and SiO_2 ($n \sim 1.45$) results in large field penetration depth, limiting the achievable mode volume [63].

The maximum finesse previously reported ($\mathcal{F} \sim 5000$ [19, 37, 41]) was limited primarily by residual absorption in the a-Si layers. Notably, however, due to the higher index contrast ($n \sim 3.7$ for a-Si), this was achieved using 4.5 period mirrors with overall thickness $\sim 1.7\,\mu$m. Furthermore, low field penetration into these mirrors enables fundamental mode volumes on the order of $1.3\lambda^3$ [41]. Another benefit is that the a-Si/SiO_2-based mirrors provide a broad omnidirectional reflection band for propagating waves incident from an external air or vacuum medium. We recently [8] showed that this omnidirectional property confers significant potential to isolate emitters from free-space radiation modes.

In the past several decades, the integrated optics community has extensively studied hydrogenated amorphous silicon (a-Si:H) as a near infrared (NIR) wave-guide material [89–97], especially for backend integration with electronics. Its attributes include potential for low-temperature deposition and processing, high refractive index ($n \sim 3.5$), and significantly reduced loss, compared to a-Si, for wavelengths longer than $\sim 700\,\text{nm}$ in the NIR region [98]. Here, we theoretically study a-Si:H as an alternative high-index thin-film material for the QWS mirrors employed in 'open-access' micro-cavities. We first provide a review of recently reported results for the absorption and scattering losses of highly optimized a-Si:H films. We then describe a theoretical study of buckled dome microcavities [41], comparing the use of a-Si:H/SiO_2 and Ta_2O_5/SiO_2-based QWS mirrors. The results suggest that a-Si:H-based mirrors could be favourable, not only at 1550 nm wavelength, but also in the $\sim$ 800 nm wavelength region that is traditionally of interest to cavity QED studies.

5.2 Optical properties of optimized a-Si:H

It is well known (see for example [98]) that incorporating the appropriate amount of hydrogen ($\sim$10 atomic %) into a-Si films can significantly reduce their optical loss in the near infrared region, through passivation of silicon dangling bonds. Too much hydrogen, however, can lead to hydrogen clustering, void formation, and high scattering losses. Several research groups have investigated a-Si:H as a platform for back-end optical interconnects on CMOS chips [90, 91, 93–97]. That work targets essentially the same requirements as needed for cQED applications (*i.e.* low absorption and scattering losses in the NIR). Optimized films with absorption coefficients as low as $\sim 0.01\,\text{cm}^{-1}$ at 1550 nm and $\sim$10 cm^{-1} at 800 nm wavelength (i.e. extinction coefficients $\sim 10^{-7}$ and $\sim 10^{-4}$, respectively) have been reported (see Fig.4 of Ref. [96] for

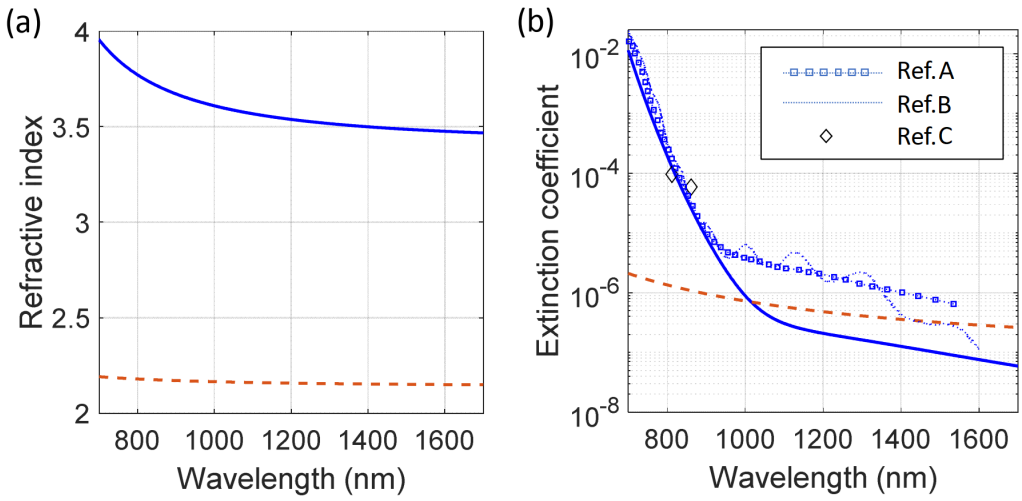

Figure 5.1: a) Refractive index and (b) extinction coefficient versus wavelength assumed for a-Si:H (blue solid curves) and Ta_2O_5 (red dashed curves) films in our modeling study. In part (b), experimental data points for a-Si:H are from the references indicated in the legend. Refs: A is [91], B is [95], C is [98]

example). These values are quite consistent with tabulated data reported in the earlier literature [98], and are competitive with many thin film materials traditionally employed in the production of optical QWS mirrors.

Our aim is to assess a-Si:H/SiO_2-based mirrors as an alternative to conventionally used Ta_2O_5/SiO_2-based mirrors for cQED applications. We employ a model for the a-Si:H optical constants (see Figure 5.1) which is derived from data reported for low-defect films in the literature [99]. Ours is essentially the model suggested by Fantoni [100], with the extinction coefficient expressed as the sum of an Urbach edge expression and a Gaussian-distributed defect expression for wavelengths above $\sim 700\,\text{nm}$. To be conservative in our predictions, we've based our fits on one of the higher-loss films, specifically the film labeled as 'Sample E' in Ref. [100]. As shown by the symbols in Figure 5.1 b), this curve agrees well, especially in the $\lambda_0 < 1000\,\text{nm}$ range, with experimental values reported by numerous research groups. The loss at longer wavelengths is known to depend on the density of defects in specific samples [98–100], but $\kappa < 10^{-6}$ at $\lambda_0 \sim 1550\,\text{nm}$ is routinely achieved, and values as low as $\kappa \sim 10^{-8}$

at λ_0 ∼1550 nm have been reported [99].

To our knowledge, reliable extinction coefficient values for Ta_2O_5 thin films have not been widely disseminated in the literature, in spite of their central role in optical thin film mirrors and filters. The curves shown in Figure 5.1 are fits to experimental data from our own Ta_2O_5 films deposited by magnetron sputtering [40]. These values are consistent with the absorption losses for highly optimized 'supermirrors' reported by various cQED researchers [20, 23, 24, 30, 63, 88].

It is important to note that our study does not directly take optical scattering into account, but implicitly assumes that the extinction coefficient encompasses both absorption and scattering. For high quality Ta_2O_5/SiO_2-based mirrors, scattering and absorption typically impart similar levels of loss in the $<$ 100 ppm range [23]. While high reflectance a-Si:H/SiO_2-based mirrors are relatively unexplored (as discussed further below), very low roughness (<0.5 nm RMS) has been achieved in multilayer a-Si:H/SiO_2 thin film stacks [94]. Moreover, the experimental data points shown in Figure 5.1(b) are based on measurements that capture both scattering and absorption contributions to the loss.

As mentioned, extinction coefficients as low as $\kappa \sim 10^{-8}$ at $\lambda_0 \sim 1550$ nm have been reported for highly optimized a-Si:H films [99, 100]. However, fabrication of QWS mirrors with such low levels of a-Si:H loss has not been demonstrated and would be challenging. Thus, we have chosen to conduct our modelling study at $\lambda_0 = 850$ nm, where there is much greater consistency in the reported loss (see Figure 5.1(b)), and where the extinction coefficient ($\kappa > 10^{-5}$) is sufficiently high to account for anticipated levels of scattering loss [23].

5.3 Comparison of a-Si:H and Ta_2O_5-based QWS mirrors

We first compare the predicted performance of QWS mirrors based on Ta_2O_5 versus a-Si:H high-index layers. We assume SiO_2 for the low index layers in both cases. Since our goal is to compare high-index materials, and since high-quality SiO_2 films typically exhibit extremely low absorption losses, we use a standard (lossless) dispersion model for the SiO_2 films ($n \sim 1.463$ and ~ 1.461 at 850 nm and 1550 nm, for example) [37, 40]. We choose a central free-space wavelength of $\lambda_0 = 850$ nm (near the D2 line of atomic cesium [63]), in order to illustrate the fact that a-Si:H confers benefits in spite of having an extinction coefficient that is more than 1 order of magnitude higher than that of Ta_2O_5 in this range. For longer wavelengths, as discussed above, it is clear that even greater advantages might be gained from using a-Si:H.

We consider (N_B-1/2-period) QWS mirrors defined by the layer sequence $(H \cdot L)^{N_B} \cdot H$, where H and L represent high- and low-index quarter-wave-layers respectively. At $\lambda_0 = 850$ nm, Figure 5.1 gives $N_T \sim 2.17 - i0.0000011$ and $N_S \sim 3.71 - i0.000036$ for the complex index of Ta_2O_5 and a-Si:H, respectively. Quarter-wave layer thicknesses of 145 nm, 98 nm, and 57 nm are used for SiO_2, Ta_2O_5, and a-Si:H, respectively. Unless otherwise indicated, we assume incidence from air ($n \sim 1$) and a fused silica exit (substrate) medium ($n \sim 1.46$). Note that the choice of exit medium does not significantly impact the main conclusions.

Many closed-form analytical expressions are available for QWS mirrors [61]. For example, neglecting loss in the low-index layers and denoting the extinction coefficient of the high index layer(κ_h), the limiting absorptance (for large N_B) can be estimated [61] by:

$$A_B \approx \frac{2\pi n_0 \kappa_h}{n_h^2 - n_l^2}, \tag{5.1}$$

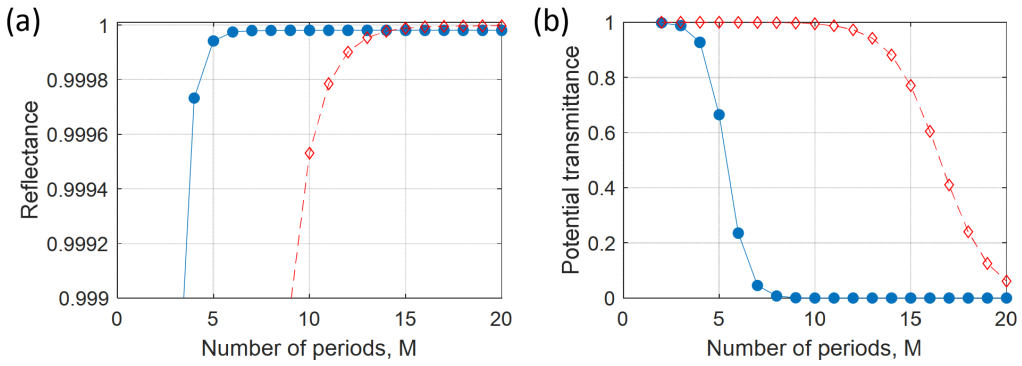

Figure 5.2: Predicted reflectance (a) and potential transmittance (b) at 850 nm wavelength versus number of periods in a QWS mirror employing a-Si:H (blue circles) and Ta_2O_5 (red diamonds) as the high-index layers.

where n_0 is the incidnet medium index, and n_h and n_l are the refractive indicies of high- and low-index layers in the QWS Now, since for any multilayer $R+T+A=1$, it follows that the maximum reflectance at the design wavelength is given by $R_\mathrm{max} \sim 1-A$. However, for QWS mirrors used in micro-cavities, $T>0$ is typically required so that photons can be coupled to an external channel. This requires a balance between R, T, and A, which is nicely encapsulated by the so-called potential transmittance $T_\mathrm{P} = T/(1-R) = T/(T+A)$. In essence, T_P is the probability that a non-reflected photon (for example, circulating in a cavity mode) is transmitted through the mirror, as opposed to being absorbed (or scattered, if A incorporates scattering as assumed here). One typical compromise is to select N_B such that $T_\mathrm{P} \sim 0.5$ (i.e. $T \sim A$ and $R \sim 1-2A$) is obtained [23, 63].

We employed standard transfer-matrix techniques to explore these tradeoffs in more detail. Figure 5.2 plots the peak reflectance and potential transmittance (at $\lambda_0 = 850\,\mathrm{nm}$) versus period count for both types of mirrors considered. Note that the a-Si:H-based mirrors attain R_max for $N_\mathrm{B}\sim 7$ whereas the Ta_2O_5-based mirrors require $N_\mathrm{B}\sim 18$ to attain R_max. Having said that, R_max is somewhat higher for the Ta_2O_5-based mirrors, as expected due to their

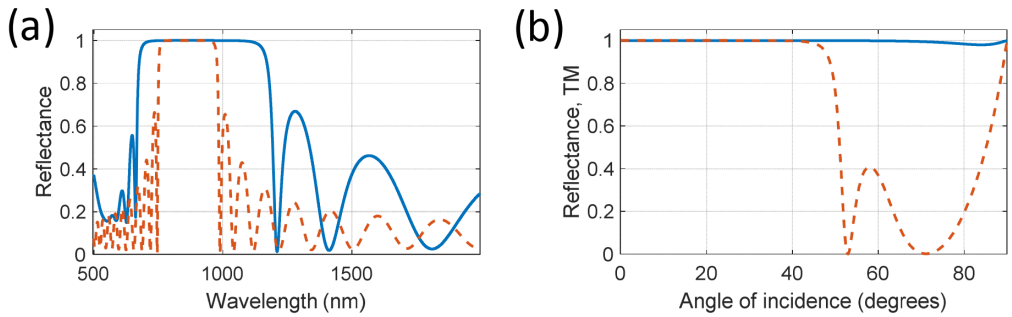

Figure 5.3: (a) Predicted normal-incidence reflectance for the 5-1/2-period a-Si:H-based (blue solid line) and 13-1/2-period Ta_2O_5-based QWS mirrors. (b) Reflectance for TM-polarized light versus incident angle at the design wavelength $\lambda_0 = 850\,\text{nm}$, for the a-Si:H- (blue solid line) and Ta_2O_5-based (red dashed line) mirrors

assumed lower extinction coefficient at this wavelength. Similar levels of T_P are predicted for similar levels of R in both types of mirrors, although Ta_2O_5 offers a slight advantage, also as expected. For the sake of comparisons that follow, we will focus our attention on the $N_B = 5$ and $N_B = 13$ cases for a-Si:H and Ta_2O_5, respectively, since they are predicted to produce $T_P > 0.5$ and a similar level of reflectance ($R\sim 0.99995$) for both mirrors. Figure 5.3(a) shows the predicted normal-incidence reflectance for both types of mirrors. Due to its much higher index contrast, the a-Si:H-based mirror exhibits a wider stop band. Furthermore, as is well known [101], the a-Si:H/SiO_2 index contrast is sufficiently high to produce a wide omnidirectional stop-band (high reflectance for all incident angles from air, for both TE- and TM-polarization), whereas the Ta_2O_5/SiO_2 index contrast is not. To illustrate this, we've plotted the TM-polarization reflectance versus incident angle in Figure 5.3(b). For TM-polarized light, the Ta_2O_5-based mirror becomes essentially transparent for incident angles greater than $\sim 50°$. This has implications for the control of spontaneous emission [8], as discussed in greater detail below.

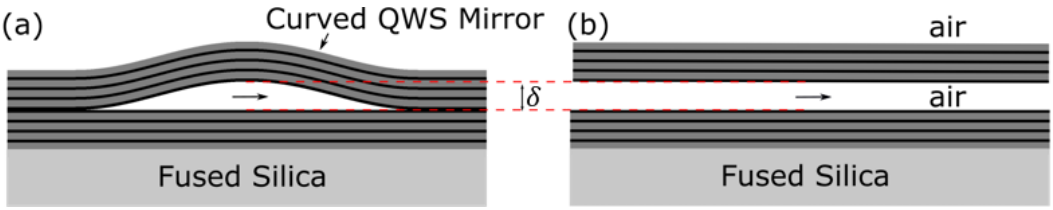

Figure 5.4: (a) Schematic diagram of a half-symmetric 'buckled dome' microcavity in cross-section, with an embedded horizontally-oriented dipole emitter indicated by the black arrow. The lower (planar) and upper (curved, with effective radius of curvature R_{oc}) mirrors are assumed to be identical N_B-1/2-period QWS (b) Planar model for the dome microcavity.

Table 5.1: Predicted model cavity parameters for operation at 850 nm wavelength as detailed in the main text

Parameter	Ta_2O_5-based	a-Si:H-based
$n - i\kappa$	$2.17 - i0.0000011$	$3.71 - i0.000036$
R	0.999955 (N_B=13)	0.999947 (N_B=5)
δ_p	172 nm	45 nm
w_0	1.83 µm	1.66 µm
Q	7.1×10^4	5.9×10^4
V_m	$3.3\lambda^3$	$1.8\lambda^3$
F_p	1.6×10^3	2.5×10^3

5.4 Comparison of spontaneous emission in a-Si:H and Ta_2O_5-based microcavities

To facilitate a numerical study of cQED effects, we use a model cavity based on our previous work [8, 41]. As shown schematically in Figure 5.4(a), the model system is a half-symmetric Fabry-Perot cavity operating in a fundamental-longitudinal-mode regime (*i.e.* $\delta \sim \lambda_0/2$)). Here, we will assume $\delta = 425$ nm, implying a cavity resonance at $\lambda_0 \sim 850$ nm for the QWS mirrors discussed in section 5.3. Furthermore, in keeping with experimental results [19, 41] , we assume a base diameter of 40 µm and an effective radius of curvature $R_{oc} = 200$ µm for the curved upper mirror. As described elsewhere [8], a simplified planar model (Figure 5.4(b)) is useful for elucidating some of the details pertaining to spontaneous emission by an embedded emitter.

Table 5.1 summarizes the predictions for our model cavity based on the

equations in Chater 2, comparing the Ta_2O_5- and a-Si:H-based cavities. For the fundamental-spatial mode cavities under consideration, $Q \sim \mathcal{F} \sim \pi/(1 - R)$, where $\mathcal{F}$ is the reflection finesse (*i.e.* we neglect any defects that would further reduce finesse), and R is the mirror reflectance The primary conclusion is that the higher index contrast of the a-Si:H-based mirrors would enable a smaller mode volume, which, in spite of a slightly lower predicted Q, results in higher F_p. These conclusions are supported by the numerical results that follow.

5.4.1 Numerical results for planar cavities

As mentioned, the high-index-contrast a-Si:H-based mirrors exhibit an omnidirectional reflection property. This in turn confers additional advantages over those already cited, related to the control of spontaneous emission by an embedded emitter [102]. To compare the two mirror systems on these merits, we first considered a planar model for the dipole-embedded cavity (Figure 5.4(b)), and applied a Green's function formalism [103] described in our previous work [8]. This planar model provides insight into the so-called background emission rate γ_{BG}, which is the rate of emission by the dipole into non-cavity modes, including radiation into free-space propagating modes through the imperfect mirrors and radiation into waveguide modes supported by the QWS multilayers.

Consider the planar version of the cavity from above (i.e. $\delta = \lambda/2$, operating in a fundamental longitudinal mode order) and with a horizontally aligned dipole embedded at the midpoint between the mirrors. Figure 5.5 shows typical plots of the predicted 'local density of modes (LDOM) density' plotted versus the in-plane component of the wavevector. The background emission rate, relative to the free-space emission rate of the dipole, can be estimated by integration of these types of curves at 'off-resonance'

wavelengths [8]. Note that modes in the range ($k_{\|}/k_0 < 1$) represent radiation into free-propagating plane waves in the air superstrate. The modes labeled as 'guided modes' actually include both leaky guided modes (substrate radiation modes) for ($1 < k_{\|}/k0 < 1.463$) and truly guided modes for ($k_{\|}/k0 > 1.463$). The data in Figure 5.5 is for $\lambda_0 = 860\,\text{nm}$ and a cavity with $\delta = 425\,\text{nm}$, such that no cavity mode is supported. From integration of these curves, we find $\gamma_{\text{BG}}/\gamma_0 \sim 0.235$ and $\gamma_{\text{BG}}/\gamma_0 \sim 0.033$ for the Ta_2O_5-based and a-Si:H-based cavities, respectively. Thus, as discussed further below, the a-Si:H-based cavity is approximately 7x better at inhibiting background emission by the optimally positioned dipole emitter. The reasons that the a-Si:H-based cavity is able to better suppress background emission can be traced to the higher index contrast of the QWS mirrors. First, their omnidirectional nature suppresses nearly all radiation into free-space propagating modes, whereas the Ta_2O_5-based mirror allows some 'leakage' of TM-polarized light in particular (see Figure 5.3(b) and Figure 5.5(a)). Second, the evanescent field of the in-plane guided modes supported by the a-Si:H QWS is much weaker at the location of the dipole, due to the stronger confinement of these modes in the a-Si:H layers compared to the Ta_2O_5 layers. This results in lower coupling to in-plane guided modes for the a-Si:H cavity, as apparent by comparison of Figure 5.5(a) and (b)

5.4.2 Numerical results for 3-dimensional cavities

To obtain a more complete picture of the impact of alternative mirrors on spontaneous emission, we performed 3-D numerical simulations with a commercial FDTD software package (Lumerical). A dipole source was located precisely in the center of the air core, to maximize coupling to the fundamental mode, and to minimize background emission into the in-plane guided and leaky modes discussed above.

As in our previous work [8], we employed the built-in feature of the FDTD

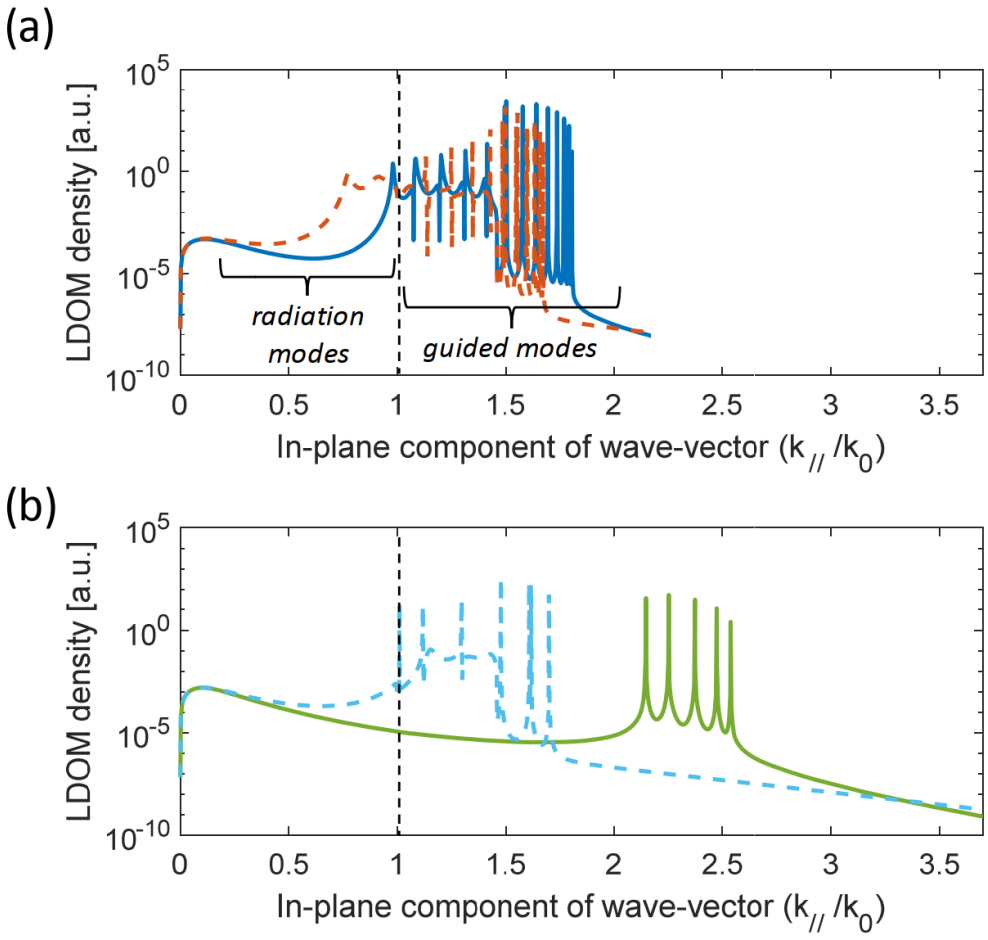

Figure 5.5: Local density of modes (LDOM) density plots versus in-plane wave-vector component, for transverse electric (TE) (solid lines) and transverse magnetic (TM) (dashed lines) polarization. The simulations were performed at an off-resonant wavelength $\lambda_0 = 860\,\text{nm}$. (a) Results for the Ta_2O_5-based cavity, predicting significant radiation into both free-space propagating ($k_\parallel/k_0 < 1$) and QWS guided modes. (b) Results for the a-SI:H-based cavity, showing that radiation into free-space modes is negligible and radiation into guided modes is reduced.

software to calculate the emission rate of an embedded dipole relative to its free-space emission rate (*i.e.* γ/γ_0), as a function of frequency. Since the dipole source is spatially aligned to the anti-node of the fundamental cavity mode in our simulations, we expect the relative emission rate at the fundamental resonance frequency to be approximately equal to the ideal Purcell factor F_p predicted in Chapter 2. Conversely, the off-resonance relative emission rate is a measure of the inhibition of background radiation, and can be assessed against the predictions from the planar model in subsection 5.4.1. It is worth noting that the accurate determination of these relative emission rates requires that the FDTD simulation runs for a sufficiently long time such that the field values have decayed to a negligible level. Since the cavities considered here have relatively long photon lifetimes ($\sim$30 ps), very long simulation times were needed (for example, up to $\sim$1 week on a multi-CPU workstation). Nevertheless, the simulations were repeatable, stable, and well-behaved.

Key results from the FDTD simulations, for both the Ta_2O_5-based and a-Si:H-based cavities, are summarized in Figure 5.6. From a comparison of Figure 5.6 (a) and (c), significantly higher spatial confinement is apparent for the a-Si:H case. The numerically predicted mode volumes are $\sim 3.5\lambda^3$ and $\sim 1.9\lambda^3$, respectively, in good agreement with the analytically predicted values. Furthermore, the numerically predicted Q-factor values for the fundamental cavity resonance are $\sim 7.9 \times 10^4$ and $\sim 6.7 \times 10^4$, respectively, also in good agreement with predictions above (slightly higher due to the air superstrate in the FDTD model).

Relative emission rates are plotted versus free-space wavelength in Figure 5.6(b) and (d). Both the on-resonance values, $\sim$1800 and $\sim$2500 respectively, and the off-resonance values, $\sim$0.24 and $\sim$0.036 respectively, provide very good corroboration of the predictions from the beginning of this section. Residual oscillations in the Purcell factor plots (visible in the insets of Fig-

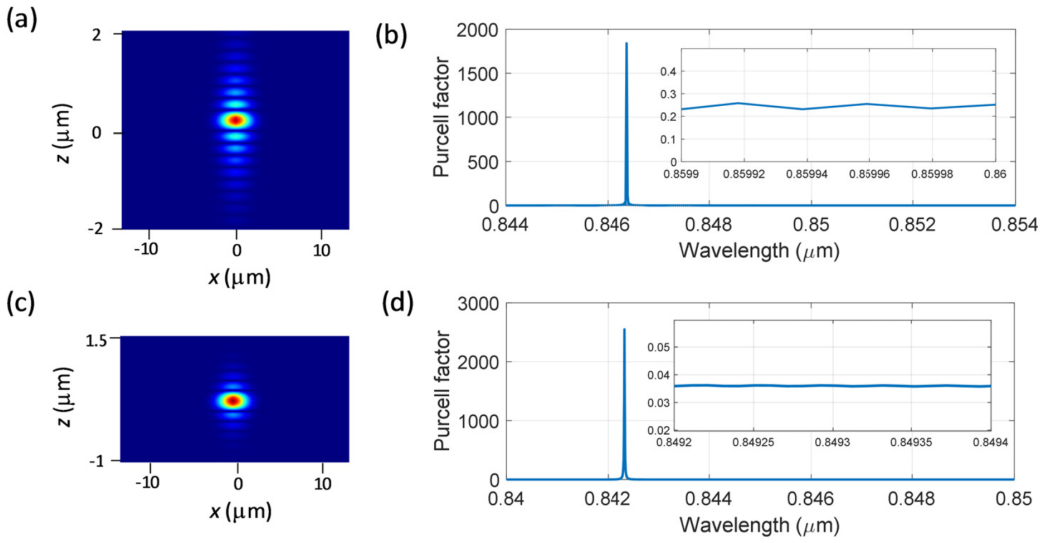

Figure 5.6: (a) Mode field intensity for the fundamental mode of the Ta_2O_5-based cavity. (b) Relative dipole emission rate versus wavelength for the Ta_2O_5-based cavity. The inset is a zoomed-in portion of the plot, far removed from the resonance. (c), (d) Show analogous plots for the a-Si:H-based cavity.

ure 5.4(b) and (d)) are a numerical artifact due to the termination of the simulation prior to complete field decay (the 'simulation time' was set to 300 ps, which is approximately 10 times the resonant photon lifetime). Overall, the FDTD results confirm the main conclusions from above: *i.e.* the a-Si:H-based mirrors enable a higher Purcell factor, primarily due to reduced mode volume, and a significantly better suppression of emission into background radiation modes. A key figure of merit for cQED is the so-called single-atom cooperativity $C = \gamma_c/(2\gamma_{BG})$, where $2\gamma_c$ and $2\gamma_{BG}$ are the rates of emission into the desired cavity mode and the background modes, respectively, for an atomic transition that is spectrally aligned (*i.e.* resonant) with the cavity mode [9]. Often, the background emission rate is approximated by the free-space emission rate (*i.e.* $\gamma_{BG} \sim \gamma_0$), which is appropriate when the cavity does not significantly inhibit emission into non-cavity modes, and in such cases $C \sim F_p/2$. However, we previously suggested [8] that for cavities that do provide significant isolation of the emitter from free-space modes, a more appropriate

definition is $C = F_{\mathrm{p}}F_{\mathrm{I}}/2$, where $F_{\mathrm{I}} = \gamma_0/\gamma_{\mathrm{BG}}$ is a so-called inhibition factor. For the scenarios discussed above, $F_{\mathrm{I}}{\sim}4.3$ and ${\sim}30.3$ for the Ta_2O_5-based and a-Si:H-based cavities, respectively. When combined with the estimated F_{p} values, $C{\sim}3500$ is predicted for the Ta_2O_5 case, while $C{\sim}38\,000$ is predicted for the a-Si:H case. It is important to keep in mind that these values pertain to an optimally aligned emitter, which would not be trivial to achieve in practice. Nevertheless, the order-of-magnitude higher predicted value of C for the a-Si:H cavities illustrates their strong potential to enhance interactions between an emitter and a single cavity mode, which is a typical goal in cQED applications.

Chapter 6

Conclusion and Future Work

6.1 Summary

The primary focus of this thesis was to monolithically fabricate Fabry-Perot micro-cavities with 'open-access', small mode-volume, and a high quality-factor. Existing fabrication techniques have limitations either in the defect finesse, mode-volume, open-access, or scalability. Open-access cavities are of particular interest to cQED applications due to access to the maximum field location.

As outlined in Chapter 3, open-access devices were fabricated by modifying a pre-buckled device (*e.g.* in Ref [5]) with through-holes patterned using photolithography and etched using RIE. Devices with dome-base diameter of 50 µm and 100 µm were successfully fabricated, and devices with dome-base diameter of 100 µm showed a high level of cylindrical symmetry and agreement to the profile predicted by elastic buckling theory. Several device configurations showed significant deviation from the predicted profile, with a general trend toward more deviation when more material was removed from the devices. The location of the etch holes relative to the dome periphery was found to affect the device morphology significantly, with a location approximately midway between the dome center and periphery resulting in the smallest deviation. Amongst the patterns studied here, the preferred device configuration

was identified as: dome-base diameter of 100 µm, pattern diameter of 40 µm, and hole diameter of 4 µm.

Chapter 4 discusses the results of the optical transmission spectroscopy performed on the 'open-access' buckled cavity devices. All devices with the preferred configuration showed a fairly high level of cylindrical symmetry and agreement with the predicted profile. All the considered devices had an experimentally extracted maximum buckle deflection ∼1.7 µm, Q >3000 and a mode-volume between 4.5 λ^3 and 4.9 λ^3. The extracted FOM from cavities which did not suffer from significant defects agreed with expected FOM, with a high projected Purcell factor (~ 75). The experimental mode-volume agrees with the predicted values, however the quality-factor showed a slight degradation with an increase in the number of holes etched. Nonetheless, devices with 3 or 6 holes showed a predicted quality factor similar to the experimental value, implying that the devices showed reflectance-limited finesse. Next, three representative devices were compared in terms of their morphology and their optical mode properties and mode structure. For all of the devices studied, having varying etch hole sizes, number, and patterns, there was a high degree of agreement with theory. Finally, we demonstrated that liquid solvents could be introduced into the cavity, producing predictable changes to the optical and spectral characteristics of the HG/LG/IG modes. While the proof-of-concept work employed 1550 nm-range mirrors, we see no significant barrier to replicating this work using our previously reported [40] buckled cavities operating in the visible and near-infrared region or with the devices simulated in Chapter 5.

In Chapter 5 we presented a theoretical analysis of buckled-cavity devices, comparing the use of conventional Ta_2O_5/SiO_2-based mirrors to the potential use of a-Si:H/SiO_2-based mirrors. Our study shows that increasing the refractive index contrast of QWS mirrors can provide important advantages for cQED applications, including potential for reduced fabrication complexity,

increased interactions between an embedded emitter and a cavity mode, and greater control over spontaneous emission. Notably, the high index contrast of a-Si:H-based mirrors can partially compensate for higher film losses, suggesting that silicon-based mirrors should be considered even in the ∼780 nm to 1000 nm wavelength range of most traditional cavity QED work.

In conclusion, the monolithically fabricated Fabry-Perot micro-cavities described in this work have confirmed open-access through fluid infiltration and shown to have a low mode-volume (∼4.5 λ^3), high quality-factor (∼5000), and therefore a high predicted Purcell factor (∼75). Similar devices were subsequently investigated in a theoretical study of silicon-based Bragg mirrors where the numerical FDTD study predicted a low-mode volume (∼1.9 λ^3), high quality factor (∼6.7×10^4), high Purcell factor (∼1800), and high idealized cooperativy (∼38 000). These devices are promising candidates for use in cQED applications.

6.2 Future work

In contrast to the extensive recent work on a-Si:H-based waveguides mentioned previously (*e.g.* Refs. [93–96]), a-Si:H/SiO_2-based multilayer Bragg mirrors are less common in the literature (although, see for example Refs. [92, 104–106]). This is possibly related to challenges associated with depositing high-quality a-Si:H and SiO_2 films by PECVD at a single temperature and in a single deposition run. However, recent work on multilayer waveguides [94] suggests that these challenges can be addressed. Another challenge associated with the use of a-Si:H as an optical material is the out-diffusion of hydrogen for temperatures above ∼200 °C [107]. This is not likely to be an issue for most cQED applications, which typically operate at or below room temperature (often at cryogenic temperatures). We submit that there are compelling reasons to pursue the development of low-loss a-Si:H/SiO_2 Bragg mirrors, and that

the ongoing refinement of deposition processes for silicon microphotonics [107] makes this goal increasingly realistic.

These 'open-access' cavities might find use for the scalable implementation of on-chip optical sensors [27, 108] and optofluidic dye laser arrays [109, 110]. Perhaps even more exciting is the prospect of using them to implement large-scale cavity QED systems envisioned for quantum information applications [22, 30, 111, 112]. Nearly all work in these areas to date has relied on hybrid-assembly. A monolithic strategy such as described here might provide significant advantages with respect to scalability and practical implementation.

References

[1] D. Stein. *Ada, a Life and a Legacy*. History of Computing Series. MIT Press, 1985.

[2] C. Fabry. "Theorie et applications d'une nouvelle methods de spectroscopie intereferentielle." In: *Ann. Chim. Ser. 7* 16 (1899), pp. 115–144.

[3] A. Perot and C. Fabry. "On the Application of Interference Phenomena to the Solution of Various Problems of Spectroscopy and Metrology." In: *The Astrophysical Journal* 9 (Feb. 1899), p. 87.

[4] C. Fabry and A. Perot. "Méthodes interférentielles pour la mesure des grandes épaisseurs et la comparaison des longueurs d'onde." In: *Ann. Chim. Phys* 16 (1899), pp. 289–338.

[5] M. Bitarafan. "Integrated Hollow-Core Microcavity Arrays - Building Blocks for Optical Sensing and Quantum Information." PhD thesis. University of Alberta, 2017.

[6] K. J. Vahala. "Optical microcavities." In: *Nature* 424 (2003), pp. 395–410.

[7] H. J. Kimble. "The quantum internet." In: *Nature* 453 (2008), pp. 1023–1030.

[8] S. Al-Sumaidae et al. "Cooperativity enhancement in buckled-dome microcavities with omnidirectional claddings." In: *Optics Express* 26.9 (2018), pp. 11201–11212.

[9] A. Reiserer and G. Rempe. "Cavity-based quantum networks with single atoms and optical photons." In: *Reviews of Modern Physics* 87.4 (2015), pp. 1379–1418.

[10] L. Giannelli et al. "Optimal storage of a single photon by a single intracavity atom." In: *New Journal of Physics* 20.105009 (2018).

[11] P. E. Barclay et al. "Coherent interference effects in a nano-assembled diamond NV center cavity-QED system." In: *Optics Express* 17.10 (2009), pp. 8081–8097.

[12] A. Faraon et al. "Coupling of nitrogen-vacancy centers to photonic crystal cavities in monocrystalline diamond." In: *Physical Review Letters* 109.3 (2012), pp. 1–6.

[13] V. S. Ilchenko and L. Maleki. "Novel whispering-gallery resonators for lasers, modulators, and sensors." In: *Laser Resonators IV* 4270.April 2001 (2001), pp. 120–130.

[14] L. He, Ş. K. Özdemir, and L. Yang. "Whispering gallery microcavity lasers." In: *Laser and Photonics Reviews* 7.1 (2013), pp. 60–82.

[15] S. Reitzenstein et al. "Low threshold electrically pumped quantum dot-micropillar lasers." In: *Applied Physics Letters* 93.061104 (2008), pp. 1–3.

[16] Z. Tu et al. "High-sensitivity complex refractive index sensing based on Fano resonance in the subwavelength grating waveguide micro-ring resonator." In: *Optics Express* 25.17 (2017), pp. 20911–20922.

[17] S. Fan Joannopoulos J. D. P. R. Villeneuve. "Photonic crystals:putting a new twist on light." In: *Nature* 386 (1997), p. 7.

[18] I. Favero and K. Karrai. "Optomechanics of deformable optical cavities." In: *Nature Photonics* 3.4 (2009), pp. 201–205.

[19] M. H. Bitarafan et al. "Thermomechanical characterization of on-chip buckled dome Fabry-Perot microcavities." In: *JOSA B* 32.6 (2015), pp. 1214–1220.

[20] G. Wachter et al. "Silicon microcavity arrays with open access and a finesse of half a million." In: *Light: Science and Applications* 8.37 (2019).

[21] S. Kuhn et al. "Nanoparticle detection in an open-access silicon microcavity." In: *Applied Physics Letters* 111.253107 (2017).

[22] L. C. Flatten et al. "Microcavity enhanced single photon emission from two-dimensional WSe2." In: *Applied Physics Letters* 112.191105 (2018).

[23] D. Hunger et al. "A fiber Fabry-Perot cavity with high finesse." In: *New Journal of Physics* 12.065038 (2010), pp. 1–23.

[24] A. Muller et al. "Fabry – Perot microcavity." In: *Optics letters* 35.13 (2010), pp. 2293–2295.

[25] C. Derntl et al. "Arrays of open, independently tunable microcavities." In: *Optics Express* 22.18 (2014), pp. 22111–22120.

[26] J. Miguel-Sánchez et al. "Cavity quantum electrodynamics with charge-controlled quantum dots coupled to a fiber Fabry-Perot cavity." In: *New Journal of Physics* 15.253107 (2013).

[27] R. K. Patel et al. "Gain Spectroscopy of Solution-Based Semiconductor Nanocrystals in Tunable Optical Microcavities." In: *Advanced Optical Materials* 4 (2016), pp. 285–290.

[28] S. W. Hoch et al. "Fiber-cavity-based optomechanical device Fiber-cavity-based optomechanical device." In: *Applied Physics Letters* 101.221109 (2012).

[29] R. Albrecht et al. “Coupling of a single nitrogen-vacancy center in diamond to a fiber-based microcavity.” In: *Physical Review Letters* 110.243602 (2013), pp. 1–5.

[30] H. Kaupp et al. “Scaling laws of the cavity enhancement for nitrogen-vacancy centers in diamond.” In: *Physical Review A - Atomic, Molecular, and Optical Physics* 88.053812 (2013), pp. 1–8.

[31] P. Romagnoli et al. “Fabrication of optical nanofibre-based cavities using focussed ion-beam milling: a review.” In: *Applied Physics B: Lasers and Optics* 126.111 (2020), pp. 1–16.

[32] S. Garcia et al. “Overlapping two standing waves in a microcavity for a multi-atom photon interface.” In: *Optics Express* 28.10 (2020), pp. 15515–15528.

[33] M. Uphoff et al. “Frequency splitting of polarization eigenmodes in microscopic Fabry-Perot cavities.” In: *New Journal of Physics* 17.013053 (2015).

[34] T. D. Barrett, T. H. Doherty, and A. Kuhn. “Pushing Purcell enhancement beyond its limits.” In: *New Journal of Physics* 22.063013 (2020), pp. 1–13.

[35] E. Epp. “Hollow Bragg waveguides fabricated by controlled buckling of Si/SiO2 multilayers.” In: *Optics express* 18.24 (2010), pp. 24917–24925.

[36] E.R. Epp. “MEMS-compatible Integrated Hollow Waveguides Fabricated by Buckling.” MA thesis. University of Alberta, 2010.

[37] T. W. Allen et al. “High-finesse cavities fabricated by buckling self-assembly of a-Si/SiO2 multilayers.” In: *Optics express* 19.20 (2011), pp. 18903–18909.

[38] T.W. Allen. “Air-core microcavities and metal-dielectric filters - building blocks for optofluidic microsystems.” PhD thesis. University of Alberta, 2012.

[39] C.A. Potts. “Integrated Devices for On-Chip Quantum Optics.” MA thesis. University of Alberta, 2017.

[40] C. A. Potts et al. “Tunable open-access microcavities for on-chip cavity quantum electrodynamics Tunable open-access microcavities for on-chip cavity quantum electrodynamics.” In: *Applied Physics Letters* 108.041103 (2016), pp. 1–5.

[41] M. H. Bitarafan and R. G. DeCorby. “Small-mode-volume, channel-connected Fabry-Perot microcavities on a chip.” In: *Applied Optics* 56.36 (2017), pp. 9992–9997.

[42] M. H. Bitarafan et al. “Bistability in buckled dome microcavities.” In: *Optics letters* 40.22 (2015), pp. 5375–5378.

[43] I. Aharonovich, D. Englund, and M. Toth. "Solid-state single-photon emitters." In: *Nature Photonics* 10 (2016), pp. 631–641.

[44] M. Vaughan. *The Fabry-Perot interferometer: history, theory, practice and applications*. CRC press, 1989.

[45] W. Shen et al. "The effects of reflection phase shift on the optical properties of a micro-opto-electro-mechanical system Fabry-Perot tunable filter." In: *Journal of Optics A: Pure and Applied Optics* 6 (2004), pp. 853–858.

[46] M. Suter and P. Dietiker. "Calculation of the finesse of an ideal Fabry–Perot resonator." In: *Applied Optics* 53.30 (2014), pp. 7004–7010.

[47] J. Moon and A. M. Shkel. "Analysis of imperfections in a micromachined tunable-cavity interferometer." In: *Smart Structures and Materials 2001: Smart Electronics and MEMS* 4334 (2001), pp. 46–53.

[48] E. Hecht. *Optics*. Pearson, 2012. ISBN: 9788131718070.

[49] E. D. Palik, H. Boukari, and R. W. Gammon. "Experimental study of the effect of surface defects on the finesse and contrast of a Fabry–Perot interferometer." In: *Applied Optics* 35.1 (1996), pp. 38–50.

[50] J. Kotik and M. C. Newstein. "Theory of LASER oscillations in fabry-perot resonators." In: *Journal of Applied Physics* 32.2 (1961), pp. 178–186.

[51] V. Daneu, C. Sacchi, and O. Svelto. "Single transverse and longitudinal mode Q-switched ruby laser." In: *IEEE Journal of Quantum Electronics* 2.8 (1966), pp. 290–293.

[52] P. Connes. "L'étalon de Fabry-Perot sphérique." In: 19.3 (1958), pp. 262–269.

[53] M. Hercher. "Errata: The Spherical Mirror Fabry-Perot Interferometer." In: *Applied Optics* 7.5 (1968), pp. 951–966.

[54] *Gaussian beam propagation*. Accessed June 20, 2020. URL: http://toolbox.lightcon.com/tools/gaussianbeampropagation/.

[55] L. D. Dickson. "Characteristics of a Propagating Gaussian Beam." In: *Applied Optics* 9.8 (1970), pp. 1854–1861.

[56] *Hermite-Gaussian Modes*. Accessed June 20, 2020. URL: http://www.optique-ingenieur.org/en/courses/OPI_ang_M01_C03/co/Contenu_14.html.

[57] *Hermite-Gaussian Modes*. Accessed June 20, 2020. URL: http://www.optique-ingenieur.org/en/courses/OPI_ang_M01_C03/co/Contenu_13.html.

[58] M. A. Bandres and J.C. Gutiérrez-vega. "Ince-Gaussian beams." In: 29.2 (2004), pp. 144–146.

[59] A. E. Siegman. "Hermite–gaussian functions of complex argument as optical-beam eigenfunctions." In: *Journal of the Optical Society of America* 63.9 (1973), pp. 1093–1094.

[60] L. Allen et al. "Orbital angular momentum of light and the transformation of Laguerre-Gaussian laser modes." In: *Physical Review A* 45.11 (1992), pp. 8185–8189.

[61] H. A. Macleod. *Thin-film optical filters*. CRC press, 2017.

[62] H. R. Bilger, P. V. Wells, and G. E. Stedman. "Origins of fundamental limits for reflection losses at multilayer dielectric mirrors." In: *Applied Optics* 33.31 (1994), pp. 7390–7296.

[63] C. J. Hood, H. J. Kimble, and J. Ye. "Characterization of high-finesse mirrors: Loss, phase shifts, and mode structure in an optical cavity." In: *Physical Review A - Atomic, Molecular, and Optical Physics* 64.033804 (2001), p. 7.

[64] D. J. Hemingway and P. H. Lissberger. "Properties of weakly absorbing multilayer systems in terms of the concept of potential transmittance." In: *Optica Acta* 20.2 (1973), pp. 85–96.

[65] D. I. Babic and S. W. Corzine. "Analytic expressions for the reflection delay, penetration depth, and absorptance of quarter-wave dielectric mirrors." In: *IEEE Journal of Quantum Electronics* 28.2 (1992), pp. 514–524.

[66] V. B. Braginsky, M. L. Gorodetsky, and V. S. Ilchenko. "Quality-factor and nonlinear properties of optical whispering-gallery modes." In: *Physics Letters A* 137.7-8 (1989), pp. 393–397.

[67] H. Y. Ryu, M. Notomi, and Y. H. Lee. "High-quality-factor and small-mode-volume hexapole modes in photonic-crystal-slab nanocavities." In: *Applied Physics Letters* 83.21 (2003), pp. 4294–4296.

[68] Y. F. Xiao et al. "High quality factor, small mode volume, ring-type plasmonic microresonator on a silver chip." In: *Journal of Physics B: Atomic, Molecular and Optical Physics* 43.35402 (2010), p. 5.

[69] R. Coccioli et al. "Smallest possible electromagnetic mode volume in a dielectric cavity." In: *IEE Proceedings: Optoelectronics* 145.6 (1998), pp. 391–396.

[70] A. Kavokin et al. *Microcavities*. Oxford university press, 2017.

[71] H. Jansen et al. "A survey on the reactive ion etching of silicon in microtechnology." In: *Journal of Micromechanics and Microengineering* 6 (1996), pp. 14–28.

[72] M. Madou. *Fundamentals of microfabrication*. Taylor & Francis, 2003. ISBN: 9780849308260.

[73] J. W. Hutchinson, M. D. Thouless, and E. G. Liniger. "Growth and configurational stability of circular, buckling-driven film delaminations." In: *Acta Metallurgica Et Materialia* 40.2 (1992), pp. 295–308.

[74] M. W. Moon et al. "Buckle delamination on patterned substrates." In: *Acta Materialia* 52 (2004), pp. 3151–3159.

[75] P. Yeh and M. Hendry. *Optical waves in layered media*. Vol. 43. 1. New York: Wiley, 1990, p. 77.

[76] Y. M. Sabry, D. Khalil, and T. Bourouina. "Monolithic silicon micromachined free-space optical interferometers onchip." In: *Laser & Photonics Reviews* 9.1 (2015), pp. 1–24.

[77] D. R. McKean et al. "Thick film positive photoresist: Development and resolution enhancement technique." In: *Journal of Vacuum Science & Technology B: Microelectronics and Nanometer Structures Processing, Measurement, and Phenomena* 13.6 (1995), pp. 3000–3006.

[78] V. F. Leavers. "Which Hough Transform?" In: *CVGIP: Image Understanding* 58.2 (1993), pp. 250–264.

[79] J. W. Hutchinson and Z. Suo. "Cracking in layered materials." In: *Advances in applied mechanics*. Vol. 29. Elsevier, 1991, pp. 63–191.

[80] M. Giraud-Carrier et al. "Perforated hollow-core optical waveguides for on-chip atomic spectroscopy and gas sensing." In: *Applied Physics Letters* 108.131105 (2016), pp. 1–5.

[81] J. W. Parks et al. "Hybrid optofluidic integration." In: *Lab on a Chip* 13 (2013), pp. 4118–4123.

[82] F. Intonti et al. "Rewritable photonic circuits." In: *Applied Physics Letters* 89.211117 (2006), p. 3.

[83] K. Dietrich et al. "Optical modes excited by evanescent-wave-coupled PbS nanocrystals in semiconductor microtube bottle resonators." In: *Nano Letters* 10 (2010), pp. 627–631.

[84] A. Casas Bedoya et al. "Reconfigurable photonic crystal waveguides created by selective liquid infiltration." In: *Optics Express* 20.10 (2012), pp. 11046–11056.

[85] A. Mech et al. "Sensitized NIR erbium(III) emission in confined geometries: A new strategy for light emitters in telecom applications." In: *Journal of the American Chemical Society* 132 (2010), pp. 4574–4576.

[86] H. Walther et al. "Cavity quantum electrodynamics." In: *Reports on Progress in Physics* 69 (2006), pp. 1325–1382.

[87] H. Mabuchi and A. C. Doherty. "Cavity quantum electrodynamics: Coherence in context." In: *Science* 298 (2002), pp. 1372–1377.

[88] L. Greuter et al. “A small mode volume tunable microcavity: Development and characterization.” In: *Applied Physics Letters* 105.121105 (2014), p. 5.

[89] R. Y. Tsai, L. C. Kuo, and F. C. Ho. “Amorphous silicon and amorphous silicon nitride films prepared by a plasma-enhanced chemical vapor deposition process as optical coating materials.” In: *Applied Optics* 32.28 (1993), pp. 5561–5566.

[90] G. Cocorullo et al. “Amorphous silicon waveguides and light modulators for integrated photonics realized by low-temperature plasma-enhanced chemical-vapor deposition.” In: *Optics Letters* 21.24 (1996), pp. 2002–2004.

[91] G. Cocorullo et al. “Amorphous silicon-based guided-wave passive and active devices for silicon integrated optoelectronics.” In: *IEEE Journal on Selected Topics in Quantum Electronics* 4.6 (1998), pp. 997–1001.

[92] L. Domash et al. “Tunable and Switchable Multiple-Cavity Thin Film Filters.” In: *J. Lightwave Technol.* 22.1 (Jan. 2004,), pp. 126–135.

[93] S. K. Selvaraja et al. “Low-loss amorphous silicon-on-insulator technology for photonic integrated circuitry.” In: *Optics Communications* 282 (2009), pp. 1767–1770.

[94] J. H. Kang et al. “Low-loss amorphous silicon multilayer waveguides vertically stacked on silicon-on-insulator substrate.” In: *Japanese Journal of Applied Physics* 50.120208 (2011).

[95] S. Zhu et al. “Effect of cladding layer and subsequent heat treatment on hydrogenated amorphous silicon waveguides.” In: *Optics Express* 20.21 (2012), pp. 23676–23683.

[96] R. Takei et al. “Sub-1 dB/cm submicrometer-scale amorphous silicon waveguide for backend on-chip optical interconnect.” In: *Optics Express* 22.4 (2014), pp. 4779–4788.

[97] J. H. Kang et al. “Amorphous-Silicon Inter-Layer Grating Couplers With Metal Mirrors Toward 3-D Interconnection.” In: *IEEE Journal on Selected Topics in Quantum Electronics* 20.4 (2014), p. 8203208.

[98] E.D Palik. “Silicon (amorphus) (a-Si).” In: *Handbook of optical constants of solids*. Vol. 3. Academic press, San Diegos, 1998.

[99] J. A. Schmidt et al. “Light-induced creation of metastable defects in hydrogenated amorphous silicon studied by computer simulations of constant photocurrent measurements.” In: *Physical Review B - Condensed Matter and Materials Physics* 59 (1999), pp. 4568–4571.

[100] A. Fantoni et al. “FDTD simulation of amorphous silicon waveguides for microphotonics applications.” In: *Integrated Optics: Physics and Simulations III* 10242.May 2017 (2017), 102420U.

[101] J. N. Winn et al. “Omnidirectional reflection from a one-dimensional photonic crystal.” In: *Optics Letters* 23.20 (1998), pp. 1573–1575.

[102] W. Liang et al. “Modification of spontaneous emission in Bragg onion resonators.” In: *Optics Express* 14.16 (2006), pp. 7398–7419.

[103] H. J. W. M. Hoekstra and H. B. H. Elrofai. “Theory of optical spontaneous emission rates in layered structures.” In: *Physical Review E - Statistical, Nonlinear, and Soft Matter Physics* 71.4 (2005), pp. 1–10.

[104] H. Yoda et al. “a-Si:H/SiO2 multilayer films fabricated by radio-frequency magnetron sputtering for optical filters.” In: *Applied Optics* 43.17 (2004), pp. 3548–3554.

[105] A. Shuaib et al. “Sputtered hydrogenated amorphous silicon thin films for distributed Bragg reflectors and long wavelength vertical cavity surface emitting lasers applications.” In: *Thin Solid Films* 519.18 (2011), pp. 6178–6182.

[106] A. V. Medvedev et al. “Spherical Distributed Bragg Reflector with an Omnidirectional Stop Band in the Near-IR Spectral Range.” In: *Semiconductors* 53 (2019), pp. 901–905.

[107] A. M. Agarwal and J. Michel. “Amorphous Silicon in Microphotonics.” In: *Springer Handbook of Glass*. Springer, 2019, pp. 1483–1493.

[108] C. Vallance et al. “Open-access microcavities for chemical sensing.” In: *Nanotechnology* 27.274003 (2016), p. 7.

[109] W. Wang et al. “Optofluidic laser array based on stable high-Q Fabry-Pérot microcavities.” In: *Lab on a Chip* 15 (2015), pp. 3862–3869.

[110] D. M. Coles et al. “Diffusion-driven continuous-wave-pumped organic dye lasers.” In: *Laser and Photonics Reviews* 9.5 (2015), pp. 538–544.

[111] B. T. Walker et al. “Driven-dissipative non-equilibrium Bose–Einstein condensation of less than ten photons.” In: *Nature Physics* 14 (2018), pp. 1173–1177.

[112] T. Vogl et al. “Compact Cavity-Enhanced Single-Photon Generation with Hexagonal Boron Nitride.” In: *ACS Photonics* 6 (2019), pp. 1955–1962.

Appendix A

Mask data

In Table A.2 each cell studied is labelled with a row letter and column number which corresponds to a designation in Table A.1.

Table A.1: Results subsection and corresponding cell from Table A.2.

Sec		Group	Cell
4.2	Cavity Device Characterization	All	G-12
4.3	Optical scans of fluid-filled devices	D_{d}=50 µm	B-10
D.2	Pattern size results	D_{p}=20 µm	B-14
		40 µm	G-12
		60 µm	B-13
D.3	Hole size results	Control	G-12
		D_{h}=4 µm	G-12
		5 µm	C-13

Mask data for the mask used to fabricate all the devices presented in this thesis. Each cell contains three dimensions in µm; dome-base diameter (D_{d}), pattern diameter (D_{p}), and hole diameter (D_{h}). Each cell consist of 512 devices in 16 columns and 32 rows. Each column consists of identical devices, each row repeats the following hole number sequency twice: 0, 3, 4, 5, 6, 8, 10 and 12.

Table A.2: Mask data

	1	2	3	4	5	6	7	8	9	10	11	12	13	14	15	16
A				100	100	100	100	100	50	50	50	50	100			
				40	40	40	40	40	20	20	20	20	40			
				3	3	4	3	4	3	4	3	4	4			
B			100	100	100	100	100	100	50	50	50	50	100	100		
			60	20	40	40	40	40	20	20	20	20	60	20		
			3	3	3	4	3	4	3	4	3	4	4	4		
C	100	100	100	100	100	100	100	100	100	100	100	100	100	100	100	100
	40	40	40	40	40	40	40	40	40	40	40	40	40	40	40	40
	5	5	5	5	3	3	3	3	4	4	4	4	5	5	5	5
D	100	100	100	100	100	100	100	100	100	100	100	100	100	100	100	100
	60	60	20	20	40	40	40	40	40	40	40	40	60	60	20	20
	3	4	3	4	3	3	3	3	4	4	4	4	3	4	3	4
E	50	50	50	50	50	50	50	50	50	50	50	50	50	50	50	50
	10	10	30	30	20	20	20	20	20	20	20	20	10	10	30	30
	3	4	3	4	3	3	3	3	4	4	4	4	3	4	3	4
F	50	50	50	50	50	50	50	50	50	50	50	50	50	50	50	50
	20	20	20	20	20	20	20	20	20	20	20	20	20	20	20	20
	5	5	5	5	3	3	3	3	4	4	4	4	5	5	5	5
G			50	50	50	50	50	50	100	100	100	100	50	50		
			10	30	20	20	20	20	40	40	40	40	10	30		
			3	3	3	4	3	3	3	4	3	4	4	4		
H				50	50	50	50	50	100	100	100	100	50			
				20	20	20	20	20	40	40	40	40	10			
				3	3	4	3	4	3	4	3	4	4			

Appendix B

Fabrication notes

B.1 Alignment

The alignment marks used a Vernier scale (in micrometers) on the mask alignment, to achieve micron-scale accuracy by manual alignment. It was quickly determined that the Teflon layer was not visible through the alignment monitor. The alignment marks were etched on the bottom mirror before the LAL was patterned. This allowed for much more visible alignment marks and for an alignment process where all masks align to one marker. This furthermore allows all masks that use those alignment marks to have a common alignment, allowing for compatibility of mask sets. An example of the alignment process with an image of the monitor used for alignment can be seen in Figure B.1.

B.2 Pinned buckling

We initially etched the holes before dicing and buckling, since the whole wafer is required to properly align the LAL and the etch holes in subsequent lithography steps. Before buckling, the devices appeared identical to the first fabrication run under an optical microscope. But regardless of the heat and time used to buckle, the devices did not de-laminate from the low adhesion layer, including attempting to buckle the devices using rapid thermal annealing (RTA). Due to the anomalous behaviour of these devices, further characterization

steps were taken, including performing optical profilometer scans using ZYGO and taking SEM images using the Zeiss EVO MA10 SEM at the nanoFAB. We found that the devices had partly buckled but only where no etching had occurred and the control devices all buckled without issue. We determined that the etching step likely fixed the top mirror to the bottom mirror, making de-lamination impossible at those locations. An example of such part buckles can be seen in Figure B.2: a) A SEM image of a etched hole. The Bragg layers can be seen as alternating dark and light strips. The Teflon layer can be seen between the top and bottom mirror. b) A ZYGO scan of a dome where only the center and top right corner buckled, separated by etched holes. c) A ZYGO scan of a dome where each side of the etched holes has buckled, but the central holes have prevented further buckling.

B.3 LAL

If the LAL does not pattern well or has surface defects, it can result in the devices not buckling at all, shallow buckles, or deformed devices. Several examples of non-ideal LAL layers can be seen in Figure B.3: a) shows a buckled device with a failed lift-off. Even with the highly compromised LAL the device still buckled, but the asymmetries are visible in the interference rings in the device. b) shows another Teflon feature that is mostly patterned correctly however a ragged edge is visible. c) An SEM image of the Teflon, the ragged edge was possibly on the side walls of the PR, indicating the ragged edge in b) is due to wall deposition during LAL patterning.

B.4 Pop off

If the devices were subjected to to high temperatures or the thermal ramp was too fast the devices would 'pop-off'. A microscope of a popped off device is

shown on the far left of Figure B.4, with three images taken within 13 seconds of each other showing the unbuckled devices, some devices initiating buckling, and the devices 'popped off'. This was visible through the optical microscope set-up used to visually monitor the buckling process.

B.5 Incomplete etching

The etch results were fairly consistent, but some defects stemming from etching were observed on otherwise functional devices. In particular incomplete etching was observed on some devices as shown later in Figure B.5: a) Shows multiple holes on a dome. b) Shows a close-up of a successfully etched hole. The individual layers of the top mirror. c) Shows a close up of a unsuccessfully etched hole. This is likely due to inconsistencies in PR patterning on the buckled devices that can occur when the surface roughness is large while spinning on PR.

B.6 Open-Access

Open-access was first confirmed using a SEM image as shown in Figure B.6. To confirm open-access in etched and not damaged domes we performed the fluid infiltration experiments.

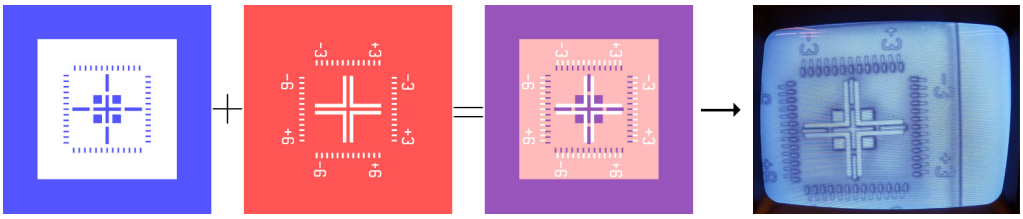

Figure B.1: Alignment marks used and an example of how it appears on a lithography alignment screen.

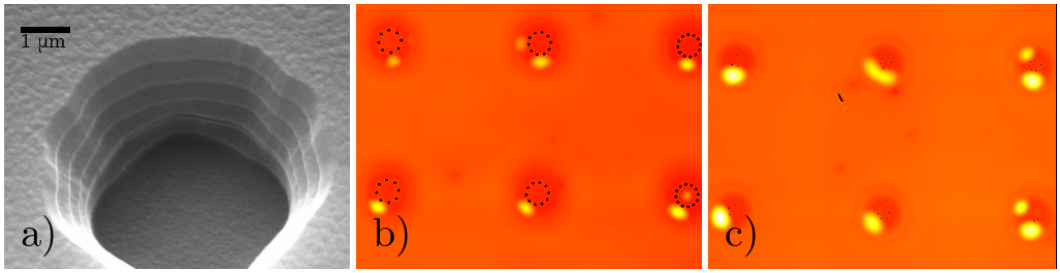

Figure B.2: Attempted buckles where you can see raised areas around the etch holes.

Figure B.3: Images related non ideal LAL layers.

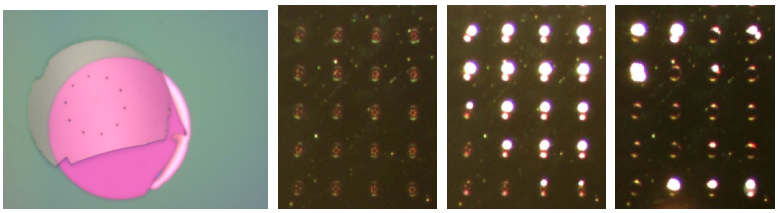

Figure B.4: Microscope images of domes during buckling and after they exploded off from being exposed to too much heat.

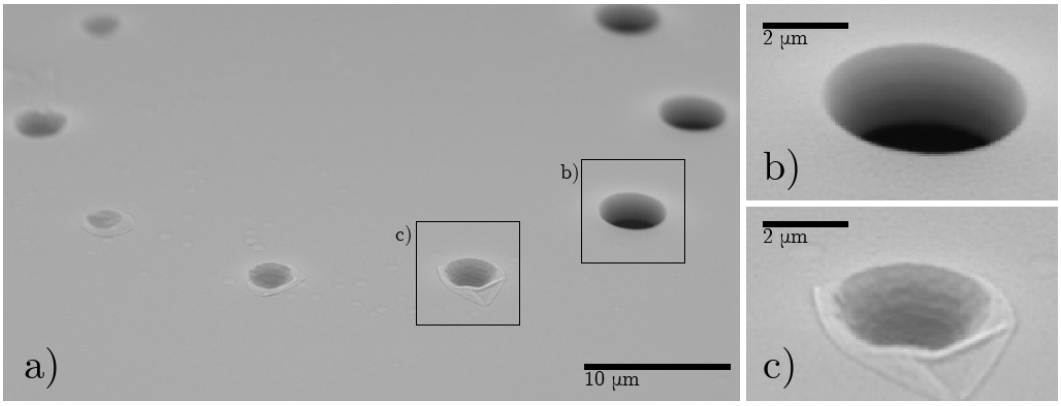

Figure B.5: Buckled dome with etch holes, some of which do not fully penetrate the dome.

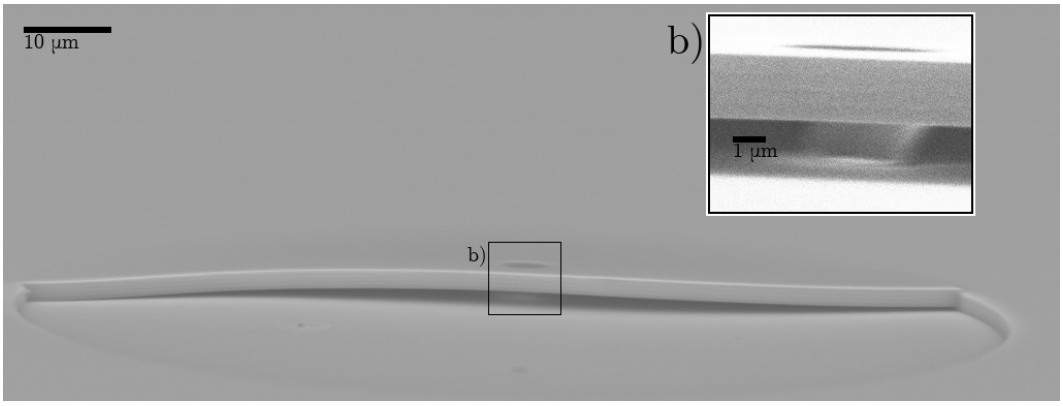

Figure B.6: Open access was first confirmed using a SEM image. Here you can see a buckled dome that was broken with the electrons passing through the etched hole.

Appendix C

Yield

To better characterise the devices on a chip scale, ZYGO profilometer scans were taken of several cells of the fabricated chip. To control for variations in film thickness and variations in temperature during de-lamination, each cell is considered independently as trenches around each cell were etched, effectively isolating the top mirror from all other cells. Each cell contained one device configuration, two sets of identical columns rotating through devices with 0, 3, 4, 5, 6, 8, 10, 12 holes and 32 identical rows give 512 devices per cell. The fabrication wafer was diced into 4 quarters, one of which only contained 3 µm devices and therefore was not etched or subsequently analysed.

The first chip that was fabricated (labeled D5) resulted in succesfully fabricated devices with D_{d} of 50 µm and 100 µm, D_{p} of $0.4D_{\mathrm{d}}$, and D_{h} of 4 µm. As in Figure C.1 the successful devices appear in a restricted area, with devices above them being mostly blown off and devices below being un-buckled. This is likely due to local variability in film thickness, poor LAL quality, and temperature variations during the buckling process. It it likely then that the high surface roughness of the LAL produced a very high critical stress of the film, but too much expansion produced cracks. The device configuration across a cell with 512 devices did not significantly affect the likelihood of a successful device, but significant discrepancies across the wafer and across a given cell

were observed.

Table C.1: Yield and average height results

D_d	D_p	D_h	Chip	Cell	Yield	Average Height	STD
50 µm	20 µm	4 µm	D5	1	9 %	0.6 µm	0.2 µm
			D5	2	44 %	0.6 µm	0.2 µm
			D5	3	42 %	0.5 µm	0.1 µm
			D5	4	88 %	0.4 µm	0.1 µm
			B	7	47 %	0.4 µm	0.1 µm
100 µm	40 µm	4 µm	D5	6	30 %	1.5 µm	0.3 µm
			A	9	91 %	1.8 µm	0.3 µm
	60 µm		B	10	37 %	1.9 µm	0.3 µm
	20 µm		B	11	32 %	2.1 µm	0.4 µm
		5 µm	B	16	51 %	2.6 µm	0.6 µm

The second fabricated chip (labelled chip B) was not fully bonded to the carrier wafer during etching. This resulted in ineffective cooling in that corner of the chip, and no devices from immediately where wasn't attached were used in the analysis that follows. Lastly a chip (labeled A) was fabricated without incident, however this mostly consisted of devices with D_h of 3 µm, and therefore they were not etched.

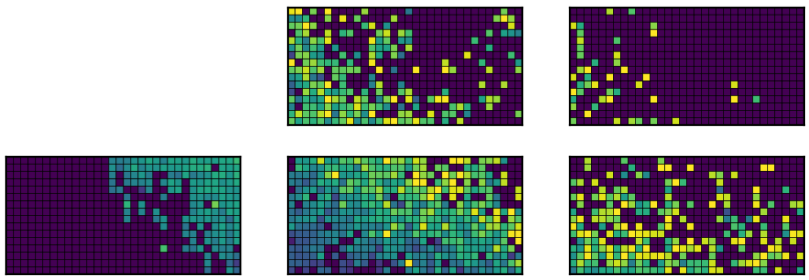

Figure C.1: This shows how the height of the domes depends more on the location of the dome than on the dome configuration with the lighter color indicating taller devices. The image is rotated for formatting reason but the cells are as follows: Top right - 1, bottom right - 2, middle top - 3, middle bottom - 4, bottom left - 6

Appendix D

Device configuration analysis

In this appendix the cavity devices will be denoted by an ID consisting of D_{d}-D_{p}-D_{h}-N_{h}. For example 100-40-4-6 denotes a 100 µm dome with a pattern diameter of 40 µm,a hole diameter of 4 µm, and 6 holes where the diameter measurements are in µm.

D.1 Further results from full device analysis

Table D.1: Measured data for different hole configurations (N_{h}) on devices with D_{d} of 100 µm, D_{p} of 40 µm, and D_{h} of 4 µm.

	Calculated Cavity Parameters	Minimum beam waist w_0 [µm]			Mode Splitting ($q = 5$)
Device ID	L [µm]	Buckling Theory	Mode Splitting	Mode Image	$\Delta\nu_{1/2}$ [GHz]
100-40-0-0	1.61	3.56	3.84	4.30	186
100-40-4-6	1.60	3.57	3.88	4.11	213
100-40-4-8	1.55	3.51	3.81	3.96	282

As a more direct comparison between the different measurement techniques the minimum beam waist of the fundamental mode was calculated using buckling theory, mode splitting, and CMOS image of the fundamental mode.

D.2 Pattern size results

We investigated the effect of the pattern size on the dome FOM. The tight, medium, and wide patterns diameter for the 100 µm diameter domes are 20 µm,

40 µm and 60 µm respectively.

In Table D.2 and Table D.3 we show results for domes with D_{d} of 100 µm, D_{h} of 4 µm, and N_{h} of 6. An image showing the relatively large amount of material removed from the tight etch pattern is shown in Figure D.1 with images of high order mode interacting with the etched holes, and lastly a microscope image showing the location of the etch holes.

Table D.2: Measured data for different pattern diameters (D_{p}) on devices with D_{d} of 100 µm, D_{h} of 4 µm, and N_{h} of 6.

	ZYGO	Spectral measurements		
Device ID	δ [µm]	ν_{q} [THz]	$\Delta\nu_{1/2}$ [GHz]	$\Delta\nu_{\mathrm{q,l,m}}$ [THz]
100-20-4-06	1.37	186.4	27.0	1.5
100-40-4-06	1.76	187.2	35.1	1.6
100-60-4-06	1.58	187.7	60.8	1.6

Table D.3: Calculated data for different pattern diameters (D_{p}) on devices with D_{d} of 100 µm, D_{h} of 4 µm, and N_{h} of 6.

	From ZYGO			From spectral measurements		
Device ID	Q	V_{m}	F_{p}	Q	V_{m}	F_{p}
100-20-4-06	4700	6.4	57	6800	4.8	109
100-40-4-06	4700	4.8	75	5300	4.6	88
100-60-4-06	4700	5.4	66	3000	4.6	51

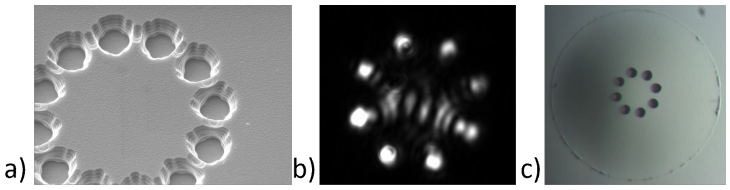

Figure D.1: Images of the tightly patterned devices. a) SEM image of the etched holes for the tight pattern. The clear overlap in the etch profiles of adjacent holes indicates a significant amount of material is removed. b) High order mode for 8 hole configuration, here the holes interfering with the mode is clear. c) Microscope image showing the same device as b) under a microscope.

D.3 Hole size results

We selected three sizes to investigate: 3 µm, 4 µm, and 5 µm . The measured and calculated data for these devices is shown in Table D.4. The control device

and the device with D_h of 4 µm show no deviation from the theoretical values.

Table D.4: Measured data for different hole sizes (D_h) on devices with D_d of 100 µm, D_p of 40 µm, and N_h of 6.

	ZYGO	Spectral measurements		
Device ID	δ [µm]	ν_q [THz]	$\Delta\nu_{1/2}$ [GHz]	$\Delta\nu_{q,l,m}$ [THz]
100-40-0-00	1.76	186.1	41.3	1.7
100-40-4-06	1.76	187.2	35.1	1.6
100-40-5-06	2.10	188.1	44.8	1.6

Table D.5: Calculated data for different hole sizes (D_h) on devices with D_d of 100 µm, D_p of 40 µm, and N_h of 6.

	From ZYGO			From spectral measurements		
Device ID	Q	V_m	F_p	Q	V_m	F_p
100-40-0-00	4700	4.8	75	4500	4.5	77
100-40-4-06	4700	4.8	75	5300	4.6	88
100-40-5-06	7000	8.8	61	4200	7.1	45